Master's Thesis

Design of MIMO Antenna for Realistic Mobile Phone Platform UsingCharacteristic Modes

Augustine Sekyere and
John Ako Enohnyaket

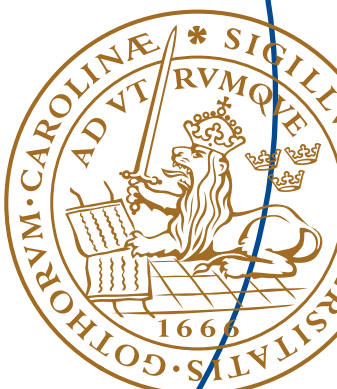

Department of Electrical and Information Technology,
Faculty of Engineering, LTH, Lund University, September 2015.

Master's Thesis

Design of MIMO Antenna for Realistic Mobile Phone Platform Using Characteristic Modes

By

Augustine Sekyere and
John Ako Enohnyaket

Department of Electrical and Information Technology
Faculty of Engineering, LTH, Lund University
SE-221 00 Lund, Sweden

Abstract

The Theory of Characteristic Modes (TCM) provides an alternative means of antenna synthesis in compact mobile handsets by taking into account the chassis. This makes it possible to create dual-element Multiple-Input Multiple-Output (MIMO) antennas in mobile handsets with very little coupling and correlation between the two antennas. But apart from the antennas, modern mobile phones are each equipped with internal components such as a touch screen, a battery, a camera and a microphone that are capable of affecting the characteristic mode behavior of the chassis. Until now, very little work has been done to study the impact of these internal components on MIMO antenna design using TCM.

In this thesis, adetailed evaluation was performed on the effects that the internal components of a mobile phone have on the characteristic modes of the antenna chassis and how these effects can be mitigated. In particular, we compared the individual eigenmodes obtained in a plain chassis structure with their corresponding (or equivalent) modes obtained after addition of the components (individually and as complete unit) and quantify the correlation between the corresponding modes.

The results show that, at frequencies lower than 1 GHz, the fundamental mode of the plain chassis structure is largely unaffected by the introduction of the internal components. On the other hand, the two modes attributed to the two T-strips on the plain chassis experienced a shift in their resonant frequencies when the internal components were introduced. However, it was found that their original resonant frequencies could be restored using minor structural changes. At higher frequencies, the introduction of the components was found to have very little impact on the characteristic modes. Finally, the chassis with all the components was employed to design a dual-band T-strip antenna, which relied on the restoration of the modal resonant frequencies to provide a broadband resonance at below 1 GHz, highlighting the usefulness of TCM analysis in antenna design.

Acknowledgments

First and foremost we like to express our sincere gratitude to God who continually sustains us and gives us strength even in difficult moments. We are also grateful to the Swedish Institute who sponsored Augustine's Education in Sweden.

Secondly, we will like to express our heartfelt gratitude to Max Landaeus who served as our industrial supervisor and the staff of Lite-On Mobile who sponsored this research and gave us unlimited access to their offices and laboratories in conducting this research.

We are also grateful to Associate Professor Buon Kiong Lau of EIT who served as academic supervisor for his immense support and guidance in carrying out this research project. We are also grateful to him for giving us the opportunity to join his research team; the invaluable experience we have acquired in interacting with his team members will go a long way to help us in our future endeavors.

Our appreciation to our co-supervisor Zachary Miers knows no bounds. His role as first point of contact for assistance helped us overcome lots of challenges. His genuine desire to help even on short notice was both refreshing and humbling.

Last but not the least, we really appreciate our family and friends who have stood by us in every stage of our life and continue to support us through prayer, support and encouragement.

Table of Contents

Preface

This thesis work was done by both Augustine and John for and on behalf of Lite-On Mobile AB in collaboration with the Department of Electrical and Information Technology (EIT) at Lund University under the supervision of Max Landaeus (Lite-On), Buon Kiong Lau (EIT) and Zachary Miers (EIT). Although this work builds upon an earlier work by Zachary Miers, none of the text, graph or data in this work was directly copied from his work. Figure 3-1 was recreated with his permission based on re-simulated data for the comparative studies. The Matlab codes used for extracting the characteristic modes were taken from the Method of Moments codes of Sergey N. Makarov that were adapted by Buon Kiong Lau and Zachary Miers. Max Landaeus provided the BetaMatch software used for the impedance matching circuit tuning in Chapter 6.

Augustine and John jointly wrote the introduction and literature review in Chapter 2. For Chapter 3, John performed the analysis for the two cases of single-component additions (camera and microphone), whereas Augustine did the analysis for the remaining three cases (screen, battery and the complete structure with all components). The work division for Chapter 4 was similar to Chapter 3, except that John also did the analysis for the complete structure. In Chapter 5, both Augustine and John took active roles in working towards the restoring the modes to the state before the addition of components. However, Augustine did the analysis for the low frequency case whereas John focused on the high frequency case. The simulations in Chapter 6 were done using the full wave Frequency Domain Solver in CST. John did the simulations and analysis for shifting the feed position and Augustine did the corresponding work for the case of varying the capacitance. Both authors worked on the high frequency simulations together. The responsibility for writing the concluding chapter was taken equally by Augustine and John.

CHAPTER 1

1 Introduction

1.1 Background and Motivation

Recent surge in the use of information technology (IT) applications such as cloud services and Bring-Your-Own Device, coupled with growing popularity of online gaming and mobile computing, calls for the provision of high data rates even in fast moving environments. However, the performance of existing coding techniques is already approaching the theoretical Shannon capacity limit, so there is little room for further improvements. Moreover, the licensing price of radio frequency spectrum is high, which limits its use for increasing data rates [1]. Thus, there is the need for a novel approach in achieving the desired high data rates. Advanced wireless technologies like Long Term Evolution (LTE) have introduced Multiple-Input Multiple-Output (MIMO) [2] as one of the key steps to achieve high data rates without the need for more spectrum or higher transmit power.

MIMO employs more than one antenna at both the transmitter and the receiver in a scattering environment to create multiple uncorrelated channels between them. This can be used to provide higher data rates, higher received signal-to-noise ratio and increased robustness to interference [1]. While employing MIMO at the base station and larger mobile devices has been done with relative ease, there remain difficult challenges in its implementation in mobile handsets [1]. This is primarily due to the compact size of mobile handsets, which allows only limited spacing among the multiple antennas. In addition, mobile handsets are equipped with many components, such as battery and touch-screens, leaving little space for antenna implementation. Thus only electrically small antennas (ESAs) are implemented in them.

In order for the ESAs to provide the desired performance requirements such as cellular band coverage, most of these antennas rely on the excitation of the mobile chassis at the desired frequencies. Chassis excitation increases the effective aperture of the small antennas. However, chassis excitation can lead

to the problem of high electromagnetic coupling and spatial correlation [1], if two or more antennas excite the same radiation mode of the chassis (often the case at frequencies below 1 GHz). This coupling and correlation problem is a lot more severe than the over-the-air coupling caused by antenna separation. Simultaneous excitation of the chassis will lead to a higher correlation of the signals from the two or more antennas in the mobile handset, thereby diminishing the benefits of MIMO. Thus antenna designers must find new ways to utilize chassis excitation in multi-antenna design while avoiding chassis-induced coupling.

The Theory of Characteristic Modes (TCM) provides a modal analysis of conductors by solving for its eigenvalues from a set of weighted eigen-function equations [3]. The eigenvalues and eigenvectors (or eigencurrents) provides valuable information about the electromagnetic properties of the conductor when excited as an antenna. While TCM was formulated back in the early 1970's [4], its role and significance in mobile handset antenna design has only recently become more prominent due to several reasons. Among them, the requirement of multi-band coverage has become very challenging, with around 40 LTE bands already planned for deployment around the world. TCM provides a systematic way to employ the chassis to provide multi-band resonances, especially since antenna implementation space is severely limited in compact mobile terminals. The TCM approach is in stark contrast with the traditional antenna design approach of mainly relying on experience and trial-and-error. Moreover, TCM conveniently provides solutions to MIMO antenna implementation, since the characteristic modes of the chassis are mutually orthogonal, which if excited by separate antennas will yield good MIMO performance.

1.2 Literature Review

Early work in the use of TCM for MIMO antenna design for mobile handset focuses on exciting multiple characteristic modes of the chassis using multiple capacitive coupling elements and a coupled feed network [5]. This approach was applied for frequency bands from around 2 GHz and above, as mobile chassis of typical sizes naturally support multiple modes at these frequencies. However, only one resonant mode can be found for mobile frequency bands below 1 GHz [6].

In order to overcome the problem of single resonant mode for the lower bands, it was discovered that additional small structures can be added to the

chassis to provide additional modes. One example is the use of two shorted strips (T-strips) on the longer sides of the chassis [6]. In [6], it was shown that the T-strips can provide additional modes, and appropriate capacitive coupling feed can be used to excite a new mode.

Subsequently, the idea was taken further to design a multi-band MIMO antenna using TCM [7]. This was achieved by correlating different characteristic currents of the chassis across different frequencies over a given feeding region, such that a given feed can be used to excite multiple resonant modes at different frequencies. These multi-resonances have been used to enhance bandwidth and provide multi-band coverage. The resulting design is capable of operating in LTE bands 5, 6 and 19 [7]. While the main antenna employed a traditional self-resonant planar inverted-F antenna (PIFA) design to excite the chassis for radiation, the secondary antenna was designed using a capacitive coupling element to effectively excite the new modes provided by the T-strips [7]. The two antennas operate with good impedance matching and more than 10 dB of isolation between them within the desired bands, which is adequate for good MIMO performance.

Furthermore, two methods were proposed in [7] to tune the multiple resonant modes that are introduced by the T-strips. The first method was by decreasing the length of the strip. This is primary due to the fact that the length of the strip serves as a capacitive load for the flow of currents. It behaves similarly to a top load dipole [7]. Thus varying the strip length affects the electrical length of the structure and subsequently its resonant frequency. The second tuning method is to vary the capacitance between the strip and chassis. This is done by adjusting the distance of separation between the strip and the chassis.

1.3 Objectives

The TCM based design in [7], though promising in terms of achieving good multi-band MIMO performance, consists of only the antennas and the plain chassis. There exist no other mobile handset components such as a screen, a camera, a microphone and a battery. Some preliminary studies performed in [6] showed that the battery and the screen did not disturb the antenna design significantly. However, the design in [6] provides only single-band coverage and was neither optimized for wideband nor multi-band coverage. Moreover, other studies such as [8] have reported potential influence of components on mobile antenna design.

Therefore, in this thesis, we investigate to study the extent to which the realistic components on mobile handset influence the TCM based design in [7] by changing the properties of its characteristic modes, as well as to find solutions that remedy the problem and restore the antenna performance.

1.4 Thesis Organization

In Chapter 2, the theory and concepts used in this thesis will be introduced. Then, the effects of adding the components on the original characteristic modes of [7] will be studied in detail in Chapters 3 and 4. In particular, the effects of adding the different components will be investigated in isolation as well as in full combination for both the low and high frequency bands. This is done by finding the envelope correlation coefficient (ECC) of each of the modes in the new structure when compared to the same modes in the original design, to determine whether there has been any changes. Chapters 5 and 6 focus on mitigating the effects from all the components on the original structure by tuning the modes to again provide wideband and multi-band resonances. This step is achieved by employing the two methods used in [7] to change the resonant frequency of a particular mode. Based on the retuned structure with the components, Chapter 7 reports on the simulation of the final design in CST to determine the antenna performance, including the bandwidth. Chapter 8 gives the conclusions from this work and provides some suggestions for future work.

CHAPTER 2

2 Theory and Concepts

In this chapter, key theories and principles that serve as the foundation for this thesis are explained. Some key papers relevant to the thesis topic are also reviewed in greater detail, in order to expand on the brief literature review given in Section 1.2.

2.1 Theory of Characteristic Modes (TCM)

A characteristic mode of a conductor refers to a specific distribution of current density around the conductor primarily due to its shape and size. This distribution is independent of external excitation [3]. The theory behind characteristic modes was first proposed by Garbacz [4] to expand on scattered and radiated fields and later refined in [9]. It explains the pattern of current distribution on the surface of the conductor and the subsequent electrical or magnetic fields formed by the current at near and far fields of the conductor surface with numerical analysis.

From [9], the characteristic mode can be expressed as an eigenvalue equation

$$[X]J_n = \lambda_n[R]J_n \tag{1}$$

where J_n is n-th modal current distribution and λ_n is the eigenvalue associated with the n-th characteristic mode. X and R are the imaginary and real component of the impedance operator Z. Since $Z = R + jX$ is both linear symmetric operator and follows reciprocity, then the eigenvalues obtained by solving (1) with moment methods are real and orthogonal [9].

Solution of equation (1) gives us the eigencurrents (J_n) and eigenvalues of the conductor. Even though the modal current distribution is independent of external excitations provided that the conductor shape and size are fixed, the eigenvalues associated with a particular modal distribution can vary over frequency. The eigenvalue $\lambda_n < 0$ implies a capacitive mode meaning the

conductor is storing electrical energy, $\lambda_n > 0$ means an inductive mode that stores magnetic energy and $\lambda_n = 0$ indicates a resonant mode [9]. Thus given a conductor with fixed shape and size, for each mode excited at different frequencies, frequency at which $\lambda_n = 0$ is termed the resonant frequency. The magnitude of λ_n gives an indication of the radiation properties of the structure. A smaller magnitude indicates a highly radiating mode. It is therefore safe to arrange the order of the characteristic modes by the order of increasing eigenvalue. The mode with the lowest resonant frequency is called the fundamental mode of the structure. This analysis approach makes TCM a valuable tool in antenna synthesis and designs [3].

Two important parameters that can be obtained from an eigenvalue analysis are the Modal Significance (MS) and the characteristic angle α_n.

MS is obtained from equation (30) in [9]. The total current (J) on the conductor surface can be expressed as

$$J = \sum_n \frac{V_n^i J_n}{1+j\lambda_n} \tag{2}$$

where V_n^i is the modal excitation coefficient that determines the effect of a particular J_n on the total current. Since smaller λ_n implies higher radiating power and higher contribution to the near and far fields, the modal significance is mathematically expressed as [3]

$$MS = \left|\frac{1}{1+j\lambda_n}\right| \tag{3}$$

Thus a particular eigencurrent with eigenvalue $\lambda_n = 0$ has the highest contribution to the overall current, and subsequently the radiated field formed by that current. At resonant frequency we can safely say that the radiated field produced by a conductor is largely due to the current density formed by the excitation.

Characteristic angle measures the phase difference between an eigencurrent and the resulting electrical field formed [3]. Mathematically

$$\alpha_n = 180° - tan^{-1}(\lambda_n) \tag{4}$$

At resonance, $\alpha_n = 180°$. A graph of characteristic angle versus frequency therefore can give an indication of the frequency at which a particular characteristic mode can be excited in a structure.

It is possible to excite another characteristic mode in addition to the fundamental mode to create MIMO antenna. The ideal mode to excite is one whose resonance frequency is closest to the resonant frequency of the fundamental mode. The excitation of a characteristic mode can be achieved either with capacitive or inductive coupling [10]. Capacitive excitation is obtained by placing the coupler at the maxima of the electric distribution (minima of magnetic distribution). Alternatively, by placing the coupler at the position maxima of magnetic distribution (minima of electric field), one achieves inductive excitation.

2.2 MIMO Antenna Design using Characteristic Modes

The focus of this section is on the design of MIMO antenna for cellular bands below 1 GHz. In [11] the chassis structure of a small mobile terminal was modified to obtain two resonant modes at frequencies below 1 GHz. The chassis dimensions were 120 mm × 65 mm. A metallic bezel added above the chassis edges and shorted to the chassis in the middle of a shorter edge generated a secondary characteristic mode. The common resonant frequency for both the fundamental and bezel modes was 0.81 GHz. Two challenges that aroused were how to generate a multi-antenna feed network to excite both orthogonal modes simultaneously and how to improve the bandwidth of the bezel mode.

From equation (2), the introduction of an external feed can modify the total current distribution on the conductor surface. Also, introducing a feed element for one mode at the wrong place can excite the second mode resulting in coupling of the current that affects MIMO performance [11]. The key to preserving the orthogonality of the two modes generated is the type and location of antenna feed [10]. The magnetic near fields *H* of the structure in [11] was analyzed in [12]. It was observed that the magnetic fields for both modes where dissimilar in the *z*-direction (i.e., H_z differs). While the fundamental mode (λ_3 as shown in Figure 1 in [12]) was dominant at center of the chassis structure, the bezel mode (λ_1 as shown in Figure 1 in [12]) was dominant at the corners of the chassis. Consequently, a folded monopole placed at the edge of the chassis was used to excite the fundamental mode, whereas an inductive coupler at the corner of the chassis to excite the bezel

mode. Both antennas resonated at 0.89 GHz, which differed from the characteristic mode resonance of 0.81 GHz [11] by 80 MHz. The key challenge to implement the simulated MIMO antenna model in [12] was to practically integrate the secondary antenna, i.e., the inductive coupler employed to excite the bezel mode. For example, impedance matching is challenging for small inductive loops and resistive losses are often high.

Following the initial results obtained in [11] and [12], new orthogonal MIMO handset antennas were designed in [6] and [7] with slight modifications to the original structure based on capacitive coupling. First two metallic strips were introduced along the long edges of the chassis structure, with the shorting pins located at the center of the strips (i.e., a "T" structure) [6]. It was observed that the width of the shorting pins as well as the height of the strips from the main chassis had an influence on both the resonant frequency and its bandwidth. Increasing the width of the shorting pin resulted in an increase in both the value and bandwidth of the resonant frequency. An increase in the height of the T-structure increased the value but decreased the bandwidth of the resonant frequency. Simulation with CST using a proper feed indicated the 6 dB impedance bandwidth of 111 MHz (868-979 MHz).

To obtain the MIMO antenna, the T-strip antenna was combined with a coupled monopole antenna (that excited the fundamental mode), which is commonly used in mobile phones. From the simulated scattering parameter results, the T-strip antenna operated within 875-965 MHz whiles the monopole operated from 809 MHz to 1 GHz [6]. The two antennas had a minimum isolation of 8.5 dB within their common bands, with isolations of up to 15 dB for frequencies lower than 935 MHz. When compared to a reference dual-antenna in [13], the new design had a total efficiency of -3.5 dB in free space and envelope correlation coefficient (ECC) of 0.07, as opposed to the -2.3 dB total efficiency and more than 0.5 ECC obtained for the reference antenna. The new antenna was found to provide a better capacity than the reference antenna in LTE Bands 8 and 5. Significantly, 1 bps/Hz higher capacity than the reference antenna was measured within LTE Band 8 [6].

The position of the user hands relative to a terminal antenna as well as the environment of the antenna can significantly alter the resonant frequency as well as the bandwidth of the antenna [8]. In [6] simulation with CST was carried out to find how the position of the user hands in two different scenarios affected the proposed MIMO antenna. In the one-hand scenario,

the efficiency of both antennas was 2 dB lower than the free space scenario within LTE Band 8. In the two-hand scenario, the efficiency of the T-strip antenna was the same as the one-hand scenario, but that of the monopole further deteriorated by 1 dB. A capacity increase of 1.5 bps/Hz was also obtained for the proposed antenna with respect to the reference antenna in the one-hand scenario. However, the proposed antenna gave a lower capacity in the two-hand scenario. It was further observed that while a battery does not have significant impact on the antenna performance, glass screens lower the resonant frequency, which is consistent to the results in [8].

A prototype of the proposed MIMO antenna in [6] was measured using a vector network analyzer and a Satimo Stargate-64 chamber. The results showed a minimum isolation of 10 dB in LTE Band 8. The efficiency was 0.5 dB lower than the CST simulated values. However, the design in [6] was single-band, which does not fulfil the requirement for multi-band coverage in modern mobile handsets.

In order to make the antenna in [6] multi-band and bandwidth-efficient, a new feeding method was proposed in [7]. The method makes use of existing feed locations (found for low frequency bands) to excite new modes at higher resonant frequencies. This is achieved by cross-correlating over a large frequency range the current distributions of the existing modes (fundamental and bezel) with other characteristic modes whose eigenvalues falls within a magnitude of 30.

It was found that two new modes within 1.3-2.0 GHz can be excited using the existing feeds. By altering a few parts of the capacitive couplers that had minimum current density, a new antenna system was designed to cover LTE Bands 5, 6, 19 and 2. Simulated results of the new design showed 6 dB impedance bandwidth within 818-896 MHz and 1841-2067 MHz as well as ECC of below 0.05. The simulated low band efficiencies were -1.6 dB and -1.2 dB for ports 1 and 2, respectively. This corresponded well with the measured -1.5 dB efficiency for the fabricated prototype. At the high band simulated efficiencies were -0.9 and -1.2 for ports 1 and 2, respectively, and the measured efficiency for the same band was -0.9 and -1.5 dB, respectively.

CHAPTER 3

3 Effects of Internal Components on Characteristic Modes at Low Frequency

To effectively study the characteristic modes, we relied on the Matlab codes designed in [14] and the use of FreeCAD (www.freecadweb.org) and in-built CAD tool in CST (www.cst.com) for the design of the components and the simulation of the antennas. In this chapter, the focus was on the effects of components on the modes at frequencies lower than 1 GHz. The higher-frequency case will be studied in Chapter 4.

The base structure that represents the chassis of a mobile phone (without any components) is a rectangular Perfect Electric Conductor (PEC) plate which has the dimensions of 120 mm × 65 mm and zero thickness, as assumed in [7]. To better appreciate the behavior of the modes, we first extracted the characteristic modes of this base structure (see Figure 3-1). By definition from TCM, these are the modes inherent in the structure, purely as a result of its shape and size. Only one mode has eigenvalue that approaches zero below 1 GHz. Recall from previous chapter that a mode is resonant if its eigenvalue equals zero. In order to obtain several resonant (or near-resonant) modes below 1 GHz, capacitance strips of dimensions 120 mm × 3.5 mm (with shorting strips of 2 mm in width) were added 3.5 mm above the two longer sides, as in [6]. λ_3 which is the fundamental modes remained unchanged and showed the same behavior and electromagnetic properties as in the case of the pure rectangular structure. However, two new modes λ_1 and λ_2 now resonate below the 1 GHz mark, as in the case in [6] and shown in Figure 3-1.

The two new modes were generated by the capacitive coupling between the rectangular structure and the capacitive strips. When a conducting object (a strip) is placed near the electrical field of another conducting object (fundamental structure), capacitance is created between the two. This has the potential to change the electrical and current properties of the fundamental structure and subsequently the characteristic modes [6]. It is therefore

concluded that λ_1 and λ_2 are produced as a result of the addition of the capacitance strips, whereas λ_3 is purely based on the size and shape of the base rectangular plate. Thus λ_3 shall be referred to as the fundamental mode. The order of numbering of the modes in the lower frequency cases is simply based on the order in which the eigenvalues approaches zero. For example, the first eigenvalue to approach zero (i.e., the mode with the lowest resonant frequency) will be denoted λ_1.

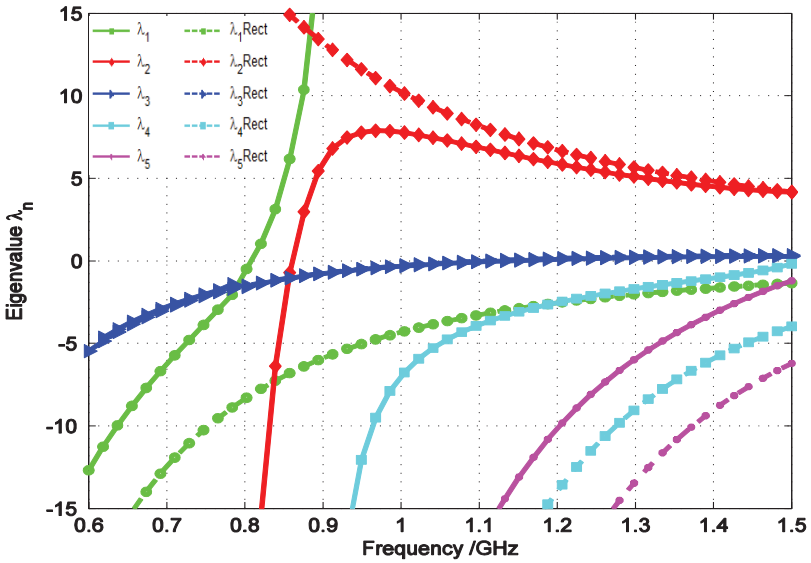

Figure 3-1. Eigenvalues of characteristic modes for a rectangular plate (REC) and a rectangular plate with metal strips (RecSTRIP).

The CAD model of the base structure with the capacitive strips and several key components inside mobile handsets was created in FreeCAD and CST. The top and bottom views of this model are shown in Figure 3-2.

In the following sections, different components (camera, microphone, battery and screen) shall be placed on the base structure, one at a time, and the effects of individual components on the characteristic modes will be analyzed. Finally the effects of adding all the components simultaneously will also be studied.

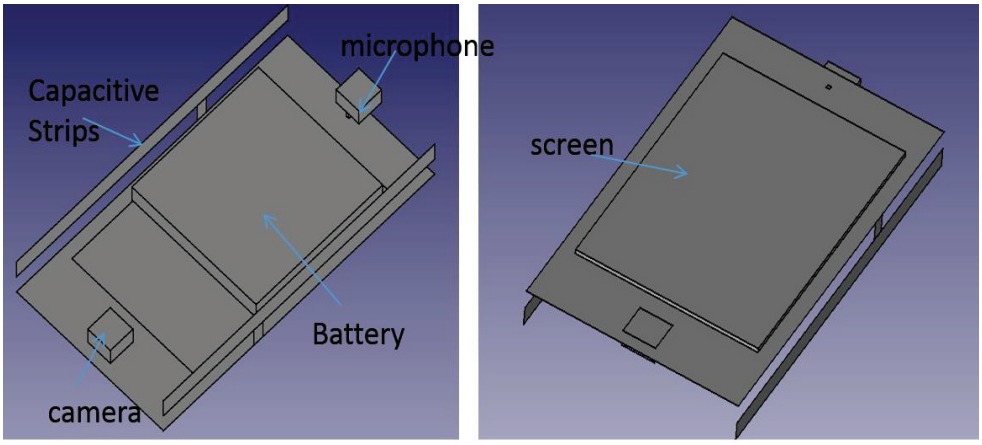

Figure 3-2. CAD model of the mobile chassis with the capacitive strips and all the components of interest added to the base structure of dimensions 120 mm × 65 mm.

3.1 Effects of the Camera on the Characteristic Modes at Low Frequency

The first component added to the capacitively-loaded rectangular chassis was the camera. It is modelled as a 10 mm × 10 mm × 3 mm structure, which was made up of 6 rectangles to form a hollow 2.5-dimensional (2.5D) structure (see Figure 3-2). It is positioned at 27.5 mm from each of the long edges and 4 mm from the shorter edge. It was placed flat on the structure without any shorting pins. **Error! Reference source not found.** and Figure 3-4 show the characteristic modes and characteristic angles of the strip-loaded base structure with the camera included.

From the graphs in Figure 3-3 and Figure 3-4, it is observed that all the eigenmode curves with the exception of λ_2 show very small deviations with the addition of the camera. This is because the presence of the camera does not increase the physical length or width of the strip-loaded base structure. λ_3, λ_4 and λ_5 were all obtained as a result of the base dimensions (120 mm x 65 mm) of the plane structure even before the introduction of the shorting pins and the capacitance strips. Hence the introduction of the camera had no effect on them. There was no significant shift in the resonant frequency of λ_1 with the introduction of the camera. However, λ_2, which was made resonant as a result of the introduction of the capacitive coupling, experienced a slight increase in the resonant frequency from 860 MHz to 870 MHz.

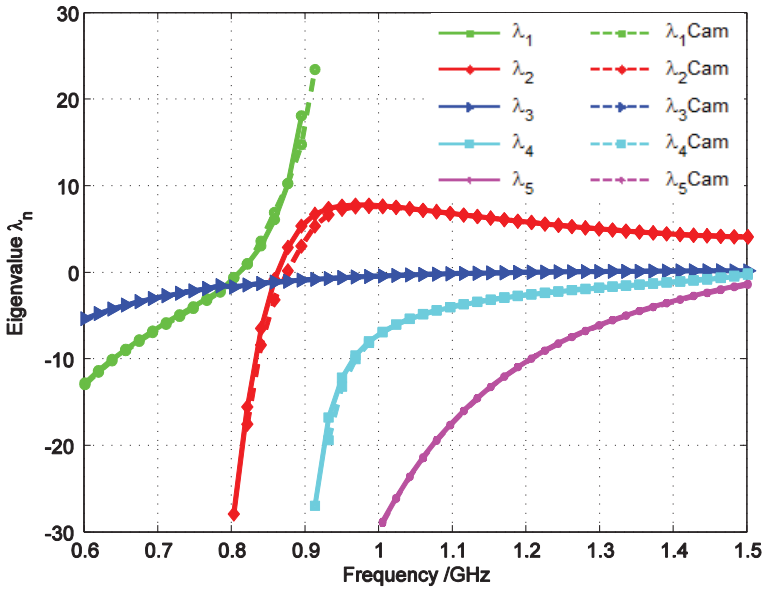

Figure 3-3. Eigenvalues of characteristic modes for the case of no components (strip loaded base structure) and the case with the addition of camera (denoted "Cam").

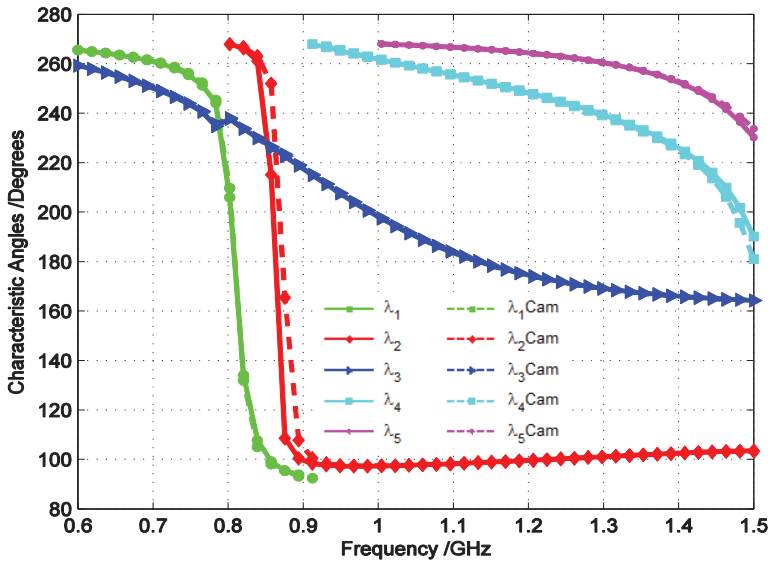

Figure 3-4. Characteristic angles of the modes for the case of no components (strip loaded base structure) and the case with the addition of camera (denoted "Cam").

As initial study, we performed further analysis on λ_2 and λ_3. While the stability of a given eigenvalue with a structural change is a strong indication that the electromagnetic properties of the mode is unchanged, we still need to investigate the mode more closely to confirm this educated guess. Moreover, in the case that the eigenvalue changes more significantly for a given mode following a structural change, it may or may not lead to significant changes in the electromagnetic properties of that mode, which also points to the need for further analysis.

To further determine the similarity between the modes (eigenvalues) obtained for the strip-loaded base structure [6], [7] and the ones obtained after the addition of the internal components, we evaluated the Envelope Correlation Coefficient (ECC) for the characteristic current distributions corresponding to the similar modes. Thus we evaluated ECC value for λ_i (i = 1, 2, 3) obtained in [6], [7] and the corresponding λ_i obtained after adding the internal component. The ECC results are summarized in Table 3-1.

Table 3-1. ECCs of eigenvalues for the addition of camera for low frequency

Characteristic modes	ECC
λ_1	0.9517
λ_2	0.9491
λ_3	0.9992

ECC values give a measure of the similarity between the two data sets on the scale of 0 to 1. 0 means no correlation (perfect orthogonality) between the two data sets and 1 means perfect correlation or the exact same data. ECC values of 0.9 or higher implies that the two modes are essentially the same and therefore they exhibit similar electrical and magnetic properties [7]. Looking at Table 3-1, it is observed that all ECC values are above 0.9 and thus all the three modes do not change appreciably with the addition of the camera. It is noted that the ECC for λ_3 was evaluated at 900 MHz, whereas those of λ_1 and λ_2 were evaluated at 850 MHz. This was done so as to obtain eigenvalues with absolute value less than 6.

The current distribution for the fundamental modes (λ_3) in the case of the camera is same as that of the strip-loaded structure without any components added. There is no interference in the current distribution of λ_3 by the camera because it is located in the current minima (area of minimum current distribution) as shown by the characteristic current distributions given in

Figure 3-5 [11]. The coordinate system used is also shown in Figure 3-5. There is high current on the longer arms of the capacitive striping but very little on the base structure (chassis). Thus the current distribution is synonymous to that of a top loaded dipole antenna placed in the y direction, as observed in [7].

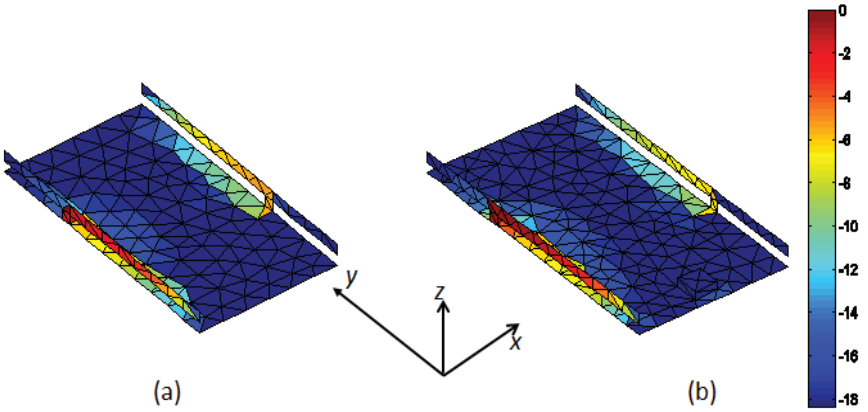

Figure 3-5. (a) Current distribution for λ_3 in the case of no component; (b) Current distribution for λ_3 in the case of adding the camera.

This observation can also be confirmed by the characteristic far field patterns corresponding to λ_3 in Figure 3-6, which shows very similar patterns with the addition of the camera (i.e., ECC value of 0.9992). As can be seen in Figure 3-6, the electric field pattern is omnidirectional in the xz-plane, and donut shaped in the other two orthogonal planes. This pattern is the same as that of an electric dipole placed along the y direction.

To further analyze the similarities of the two fundamental modes, we evaluated the dominant component (x, y or z) in the electric (E) and magnetic (H) fields in the near fields of the structure. To determine the dominant component in the E-field, we use the expression below to determine the electric energy in any given component [9]

$$\frac{\Sigma\left(abs\left(EE_i(:)\right)\right)^2}{\Sigma\left(abs\left(EE_x(:)\right)\right)^2+\Sigma\left(abs\left(EE_y(:)\right)\right)^2+\Sigma\left(abs\left(EE_z(:)\right)\right)^2} \quad . \tag{5}$$

where EE_i denotes the electric field in the i-th component (x, y or z).

Similarly, to determine the dominant H-field (denoted by HH_i), the relevant expression is [9]

$$\frac{\Sigma\left(abs\left(HH_i(:)\right)\right)^2}{\Sigma\left(abs\left(HH_x(:)\right)\right)^2+\Sigma\left(abs\left(HH_y(:)\right)\right)^2+\Sigma\left(abs\left(HH_z(:)\right)\right)^2} \tag{6}$$

In [9] the formulas for the total energy in the E- and H-fields (over a spatial region close to the structure) are given as the denominators of equations (5) and (6), respectively. The total energy in the E-field (or H-field) is obtained by summing the individual components in the x, y and z directions, respectively. Therefore it is possible to obtain the percentage contribution of each component by expressing that component as a ratio of the total field energy as shown in equations (5) and (6), respectively. The component with the highest value is then the dominant field and it gives an indication of which direction a capacitive (or inductive) coupling element should be placed in order to excite the electric (or magnetic) field of the mode. The results of this analysis is shown in Table 3-2.

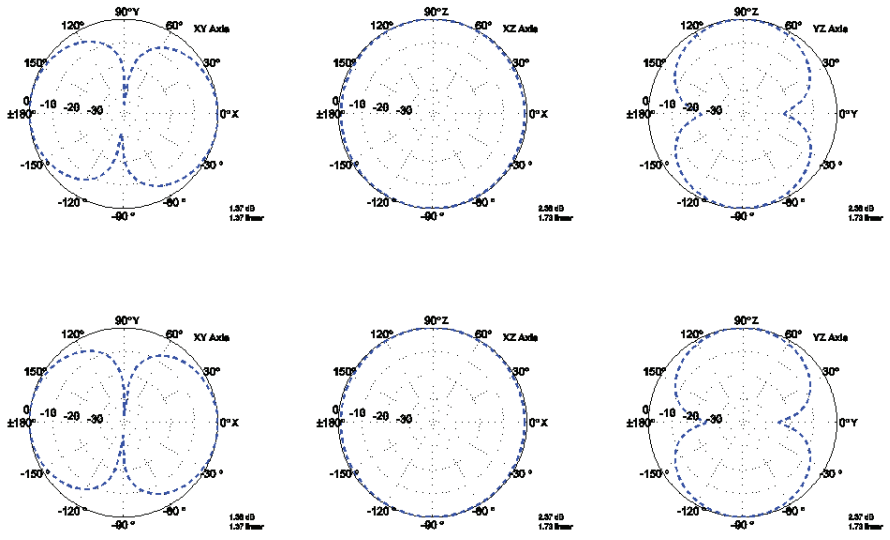

Figure 3-6. Far field pattern of λ_3 in different 2D plane: (a) xy-plane - no components (b) xz-plane - no components (c) yz-plane - no components (d) xy-plane - camera (e) xz-plane - camera (f) yz-plane – camera

Table 3-2. Estimation of the dominant components for the E and H-fields for λ_3.

	E-Field		H-Field	
Direction	No Components	Camera	No Components	Camera
x-component	0.0304	0.0324	0.9269	0.9236
y-component	0.3303	0.3032	0.0071	0.0124
z-component	0.6663	0.6644	0.0661	0.0640

From Table 3-2 we see that both cases of the base structure and the addition of the component, the z-component of the E-field for λ_3 is the dominant as it accounts for more than two-thirds of the E-filed strength. Similarly the x-component forms the dominant part of the H-field in both instances. This results is same as obtained in [17].

We can therefore conclude that the modes that do not experience any significant change in their eigenvalues and characteristic mode near and far-field patterns maintain most of their electromagnetic properties and therefore need no new analysis. This is also supported by ECC values that are close to 1 (see Table 3-1).

Comparing the case of no components to the case with camera, λ_1 and λ_2 have ECC values of 0.9517 and 0.9491, respectively. While λ_1 did not experience any significant change in the resonant frequency, λ_2 experienced about 10 MHz of increase in the resonant frequency (from 860 MHz to 870 MHz). In order to verify if the 10 MHz shift in frequency had an impact on their near and far-field properties, we evaluated the current distributions, far-field pattern, E- and H-fields in the near fields and the ECC for λ_2 before and after the addition of the camera.

As can be seen in Figure 3-7, there is no significant change in the current distribution of the two structures. There is only a small change in the intensity of the current distribution on the longer arm of the shorted strips.

Figure 3-8 shows the magnitude of the E-field distributions 3 mm above the rectangular plate. The near field pattern follows the current density pattern in Figure 3-7, i.e., higher E-field density correlates well with higher current density on the longer arms of the capacitive strips.

An analysis of the dominant component of the E- and H-fields were also performed and the results shown in Table 3-3.

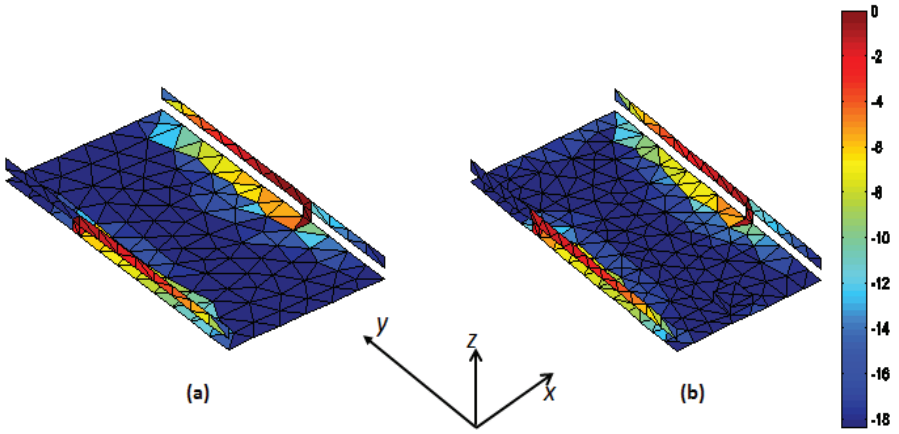

Figure 3-7. (a) Current distribution for λ_2 in the case of no components; (b) Current distribution for λ_2 in the case of adding camera.

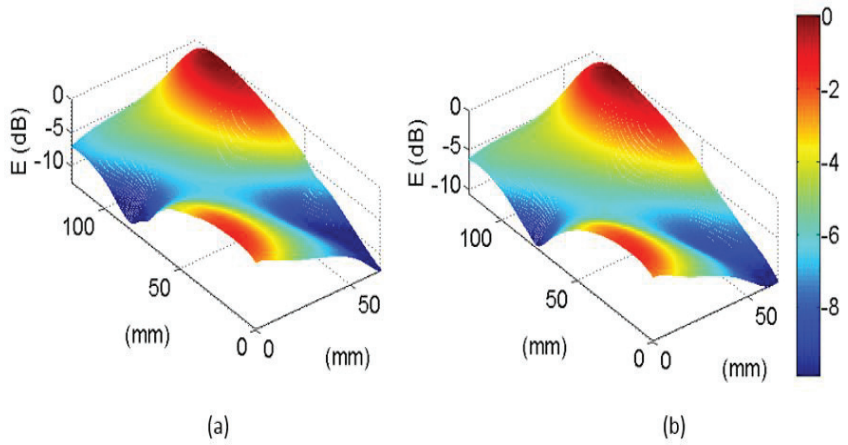

Figure 3-8. (a) E-field distribution for λ_2 in the case of no components. (b) E-field distribution for λ_2 in the case of adding camera.

Table 3-3. Estimation of the dominant components for E and H fields for λ_2.

	E-Field		H-Field	
Direction	No Components	Camera	No Components	Camera
x-component	0.5501	0.5309	0.2351	0.2313
y-component	0.0295	0.0297	0.1190	0.1517
z-component	0.4204	0.4394	0.6459	0.6169

As can be observed in Table 3-3, in both instances (without and with camera) the E-field is dominated by both the x and z-directions and the magnetic field only has a dominant component in the z-direction. This indicates that any capacitive coupler should be oriented in the x or z direction, whereas an inductive coupler should excite H-field in the z-direction.

The far-field patterns of λ_2 (without and with camera) are also shown in Figure 3-9. They resemble the pattern of a dipole antenna slightly rotated away from the y-direction within the xy-plane (diagonally positioned). This is due to the fact that the two shorting pins supporting the metal strips are not positioned exactly at the center of the longer edges on opposite sides of the plain rectangle chassis. Rather they are positioned 20 mm from the center on the opposite sides. This was done to enhance the bandwidth of λ_2 [7].

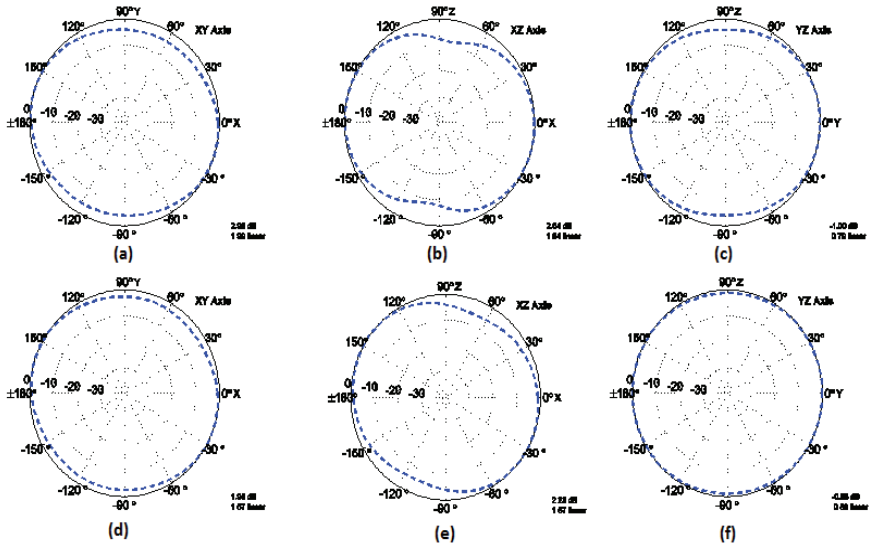

Figure 3-9. Far field pattern of λ_2 in different 2D plane: (a) xy-plane - no components (b) xz-plane - no components (c) yz- plane - no components (d) xy-plane - camera (e) xz-plane - camera (f) yz-plane - camera

3.2 Effects of the Microphone on the Characteristic Modes at Low Frequency

The previous analysis approach for the addition of a camera is repeated in this section for the addition of a microphone. The microphone was modelled as a 10 mm × 10 mm × 3 mm PEC cuboid connected via a 1 mm shorting pin

to the ground plane, on the same side of the structure as the camera (see Figure 3-2). However, it was connected near the other short edge (114 mm) as compared to the camera and it extended slightly beyond the rectangular ground plane. Thus it increased the overall length of the structure by 4 mm such that the new dimensions were 124 mm × 65 mm. The eigenvalues and characteristic angles of the structure (without and with the microphone) are shown in Figure 3-10 and Figure 3-11, respectively. The ECC values of the characteristic far-field patterns (without vs. with microphone) was calculated and shown in Table 3-4.

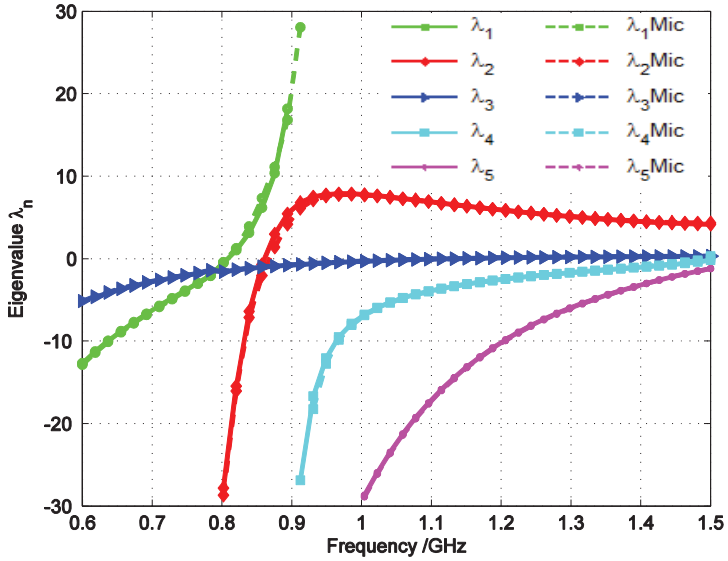

Figure 3-10. Eigenvalues of characteristic modes for the cases of no components (strip loaded base structure) and the case with the addition of microphone (denoted "Mic").

Table 3-4: ECCs of eigenvalues for the addition of microphone for low frequency.

Characteristic modes	ECC
λ_1	0.9661
λ_2	0.9526
λ_3	0.9987

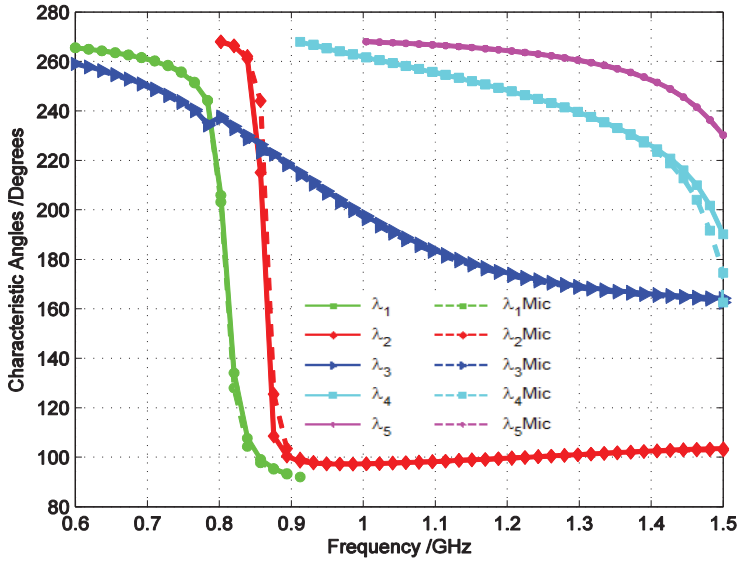

Figure 3-11. Characteristic angles of the modes for the cases of no components (strip loaded base structure) and the case with the addition of microphone (denoted "Mic").

From the structural perspective, the case of the microphone is somewhat similar to the case of the camera (i.e., the addition of a small PEC box on one short edge of the chassis). This trend is also reflected in the eigenvalues and characteristic angles, except for the shift in the resonant frequency of λ_2, which is relatively smaller in this case than that of the case with the camera. There is only a 5 MHz increase from 860 MHz to 865 MHz.

This implies there is minimal if not negligible impact on the characteristic mode properties and behavior as a result of the introduction of the microphone. This can be largely due to the fact that the microphone is only partly contained in the ground plane dimensions of 120 mm × 65 mm, and connected to the chassis only through the shorting pin. Hence it has less impact on the capacitive coupling between the two strips as compared to the camera, which was positioned directly on the ground plane and fully contained within the ground plane dimensions.

Further comparisons were made for λ_2 since it had a relatively lower ECC value when compared to the other two modes. We observed that the behavior of λ_2 is very similar to the λ_2 of the camera, in that there is higher current density on the longer arm of the capacitive strips as well as the longer edges of the fundamental structure as shown in Figure 3-12.

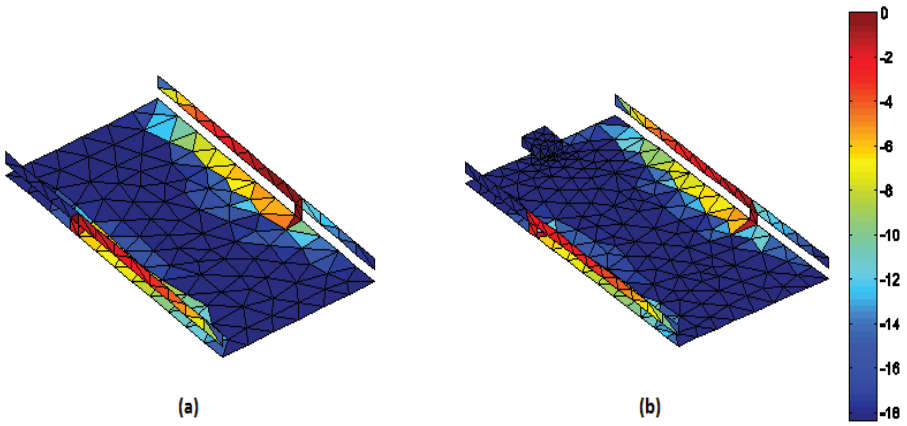

Figure 3-12. **(a)** Current distribution for λ_2 in the case of no components; (b) Current distribution for λ_2 in the case of adding microphone.

There is high current density on both the edges of the base structure and the longer edges of the metal strips. This is very similar to the current distribution of a dipole placed in the y-direction. This is further supported by the E-field distribution shown in Figure 3-13.

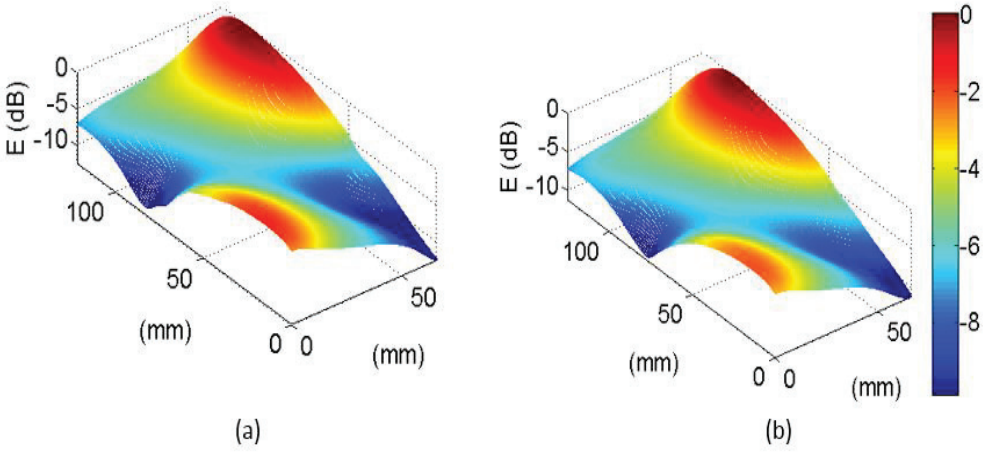

Figure 3-13. (a) E-field distribution for λ_2 in the case of no components; (b) E-field distribution for λ_2 in the case of adding microphone.

Table 3-5. Estimation of the dominant components for E and H-fields of λ_2.

	E-Field		H-Field	
Direction	No Components	Microphone	No Components	Microphone
x-component	0.5501	0.5458	0.2351	0.2349
y-component	0.0295	0.0376	0.1190	0.1946
z-component	0.4204	0.4166	0.6459	0.5705

It is observed from Table 3-5 that the introduction of the microphone slightly reduced the dominance of the x and z-components of the E-field. For the H-field, there was a slight reduction in the dominance of the z-component and a significant increase in the y-component.

Similar observations as the previous case of adding camera can be made for the far field patterns without and with the microphone shown in Figure 3-14. Namely, the patterns bear resemblance to that of a dipole antenna oriented slightly away from the y axis in the xy-plane.

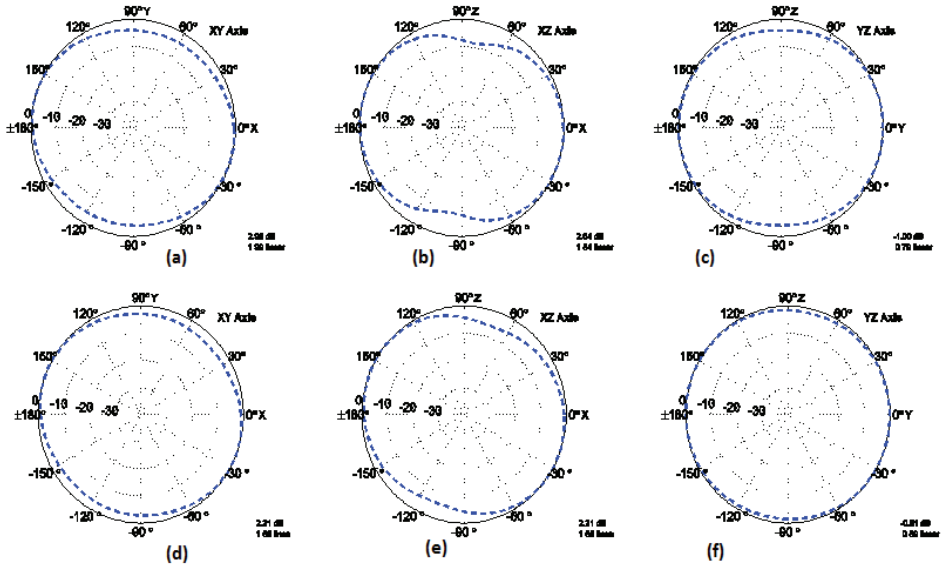

Figure 3-14. Far field pattern of λ_1 in different 2D plane: (a) xy-plane - no components (b) xz-plane - no components (c) yz- plane - no components (d) xy-plane - microphone (e) xz-plane - microphone (f) yz-plane - microphone

3.3 Effects of the Battery on the Characteristic Modes at Low Frequency

Following the same approach taken to analyze the effect of adding the camera and the microphone, the battery was modelled as a PEC box with dimensions 56 mm × 55 mm × 3 mm (see Figure 3-2). It was simulated with the strip-loaded base structure in two different ways. In the first instance, the battery was suspended 1 mm above the base structure without any connection to the rectangular ground plane, whereas in the second instance, the battery was suspended as before but now connected to the strip-loaded base structure via a 1 mm shorting pin.

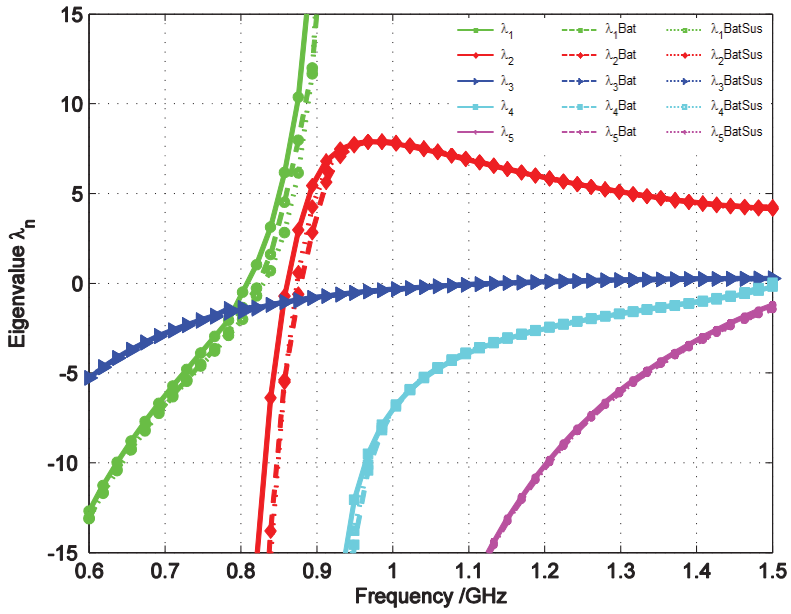

Figure 3-15. Eigenvalues of the characteristic modes for the cases of no components and the addition of battery ("Bat" denotes battery attached to ground plane, "BatSus" denotes battery suspended above ground plane).

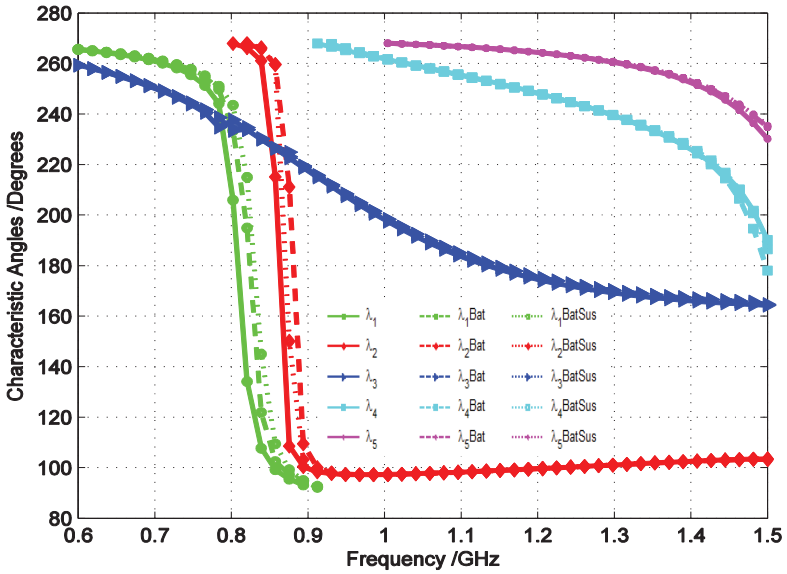

Figure 3-16. Characteristic angles of the modes for the cases of no components and the addition of battery ("Bat" denotes battery shorted/connected to ground plane, "BatSus" denotes battery suspended above ground plane).

Figure 3-15 presents the characteristic modes of the strip-loaded base structure with battery included (i.e., both cases of connected battery or suspended battery). Unlike the case of the microphone and the camera, there is a significant increase in the resonant frequency of λ_1 as well as λ_2. This is due to the fact that the battery is significantly larger than the camera and the microphone. Also, the edges of the battery in both placements are very close to the two capacitance strips, thereby interacting with the electromagnetic fields created by the metal strips. Thus we can attribute the greater increase in the resonant frequency of λ_1 as a result of the interaction between the battery and the capacitance strips. However there is very little difference between the cases of suspended battery and connected battery via shorting at their points of resonance.

Table 3-6. ECCs of eigenvalues for the addition of battery for low frequency.

Mode combination	No components vs. connected battery	No components vs. suspended battery	Suspended vs. shorted battery
ECC λ_1 - λ_1	0.9588	0.9818	0.9116
ECC λ_2 - λ_2	0.9567	0.9856	0.9191
ECC λ_3 - λ_3	0.9994	0.9998	0.9999

It can be seen from the ECC values in Table 3-6 that modelling the battery as a suspended piece without any connection to the base structure makes very little impact on the characteristic modes. This is mostly due to the fact that there is no direct current flow from the base structure to the battery; therefore the E-field properties of the base structure is largely preserved. This is confirmed by the current distribution graph shown in Figure 3-17, the case of battery suspended has a very similar current distribution to that of the case of no components.

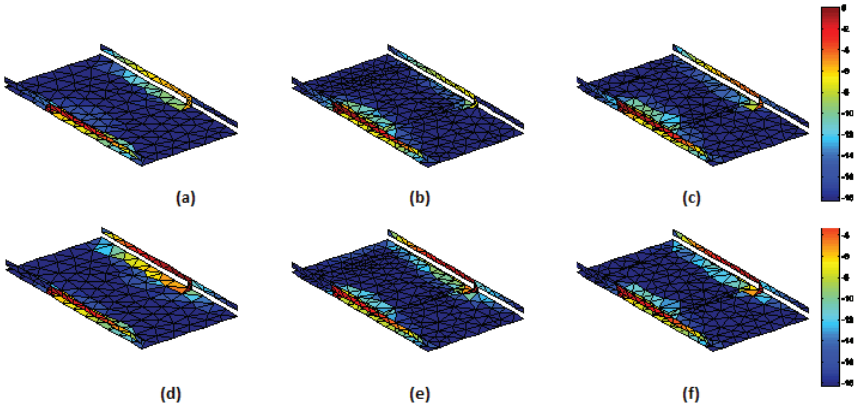

Figure 3-17. Current distributions for: (a) λ_1 - no components (b) λ_1 - shorted battery (c) λ_1 - suspended battery (d) λ_2 - no components (e) λ_2 – shorted battery (f) λ_2 - suspended battery.

The near field distribution of the E-field magnitude is shown in Figure 3-18. As can be seen by comparing Figure 3-18 with Figure 3-17, the high current density near the longer arms of the shorting pins (along the strips) corresponds well with the high E-field region, whereas the central part of the base structure has little or no current. This behavior is very similar top loaded dipole antenna.

The E-field of λ_1 is dominated by both the x and z components (see Table 3-7). However, the introduction of the battery decreased the z-component and increased the x-component. The case of suspended battery has a higher correlation to the case of no components than the case of shorted battery. This is because the shorting pin provides a direct path for current movement between the base structure and the battery. In the case of the suspended battery, there is capacitive coupling between the two parts and this has less impact on the field distribution when compared to the shorted case.

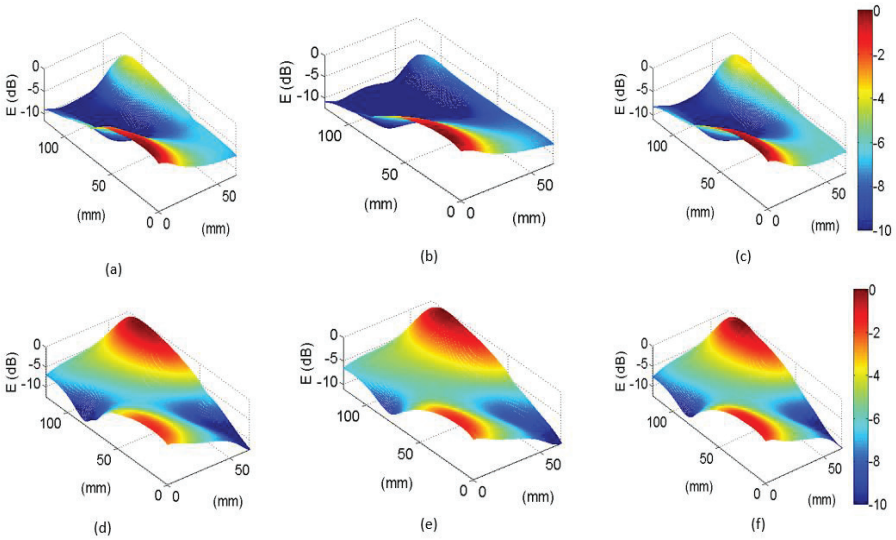

Figure 3-18. E-field magnitude distributions for: (a) λ_1 - no components (b) λ_1 – shorted battery (c) λ_1 - suspended battery (d) λ_2 - no components (e) λ_2 - shorted battery (f) λ_2 - suspended battery.

Table 3-7. Estimation of the dominant components for E- and H-fields for λ_1 and λ_2.

Direction	E-Field			H-Field		
	No components	Shorted battery	Suspended Battery	No components	Shorted battery	Suspended Battery
λ_1 x-component	0.5232	0.5594	0.5192	0.5232	0.5594	0.2165
λ_1 y-component	0.0350	0.0377	0.0345	0.0350	0.0377	0.2742
λ_1 z-component	0.4419	0.4029	0.4463	0.4419	0.4029	0.5092
λ_2 x-component	0.5501	0.5423	0.5587	0.5501	0.5423	0.2227
λ_2 y-component	0.0295	0.0262	0.0261	0.0295	0.0262	0.1142
λ_2 z-component	0.4204	0.4315	0.4152	0.4204	0.4315	0.6631

3.4 Effects of the Screen on the Characteristic Modes at Low Frequency

The last component to be added is the screen, which was modelled as a 101.6 mm hollow box 0.8 mm high. It was placed on the opposite side to the side with the two metal strips, thus increasing the overall height of the structure to 7.8 mm. The screen box was attached directly to the base structure without any connection pin, just like the camera.

Figure 3-19 and Figure 3-20 show the eigenvalues and characteristic angles of the base structure without and with the screen included. As can be seen, the screen caused a significant change in the resonant frequency of both λ_1 and λ_2. The resonant frequency of λ_1 increased from 805 MHz to 820 MHz and that of λ_2 increased from 860 MHz to 890 MHz. The ECC results of 0.9964, 0.9840 and 0.9991 were recorded for λ_1, λ_2 and λ_3 respectively (far field pattern correlation without screen vs. with screen). Thus like all other cases studied to date, the screen has essentially no impact on the fundamental mode λ_3. However, there are more significant changes in λ_1 and λ_2, which is reflected in the shift in the resonant frequency.

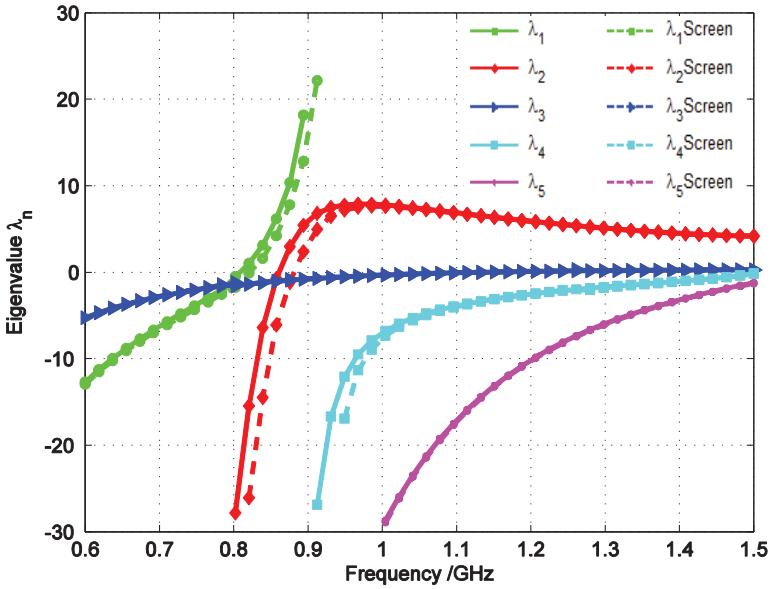

Figure 3-19. Eigenvalues of the characteristic modes for the cases of no components and the case with the addition of screen,

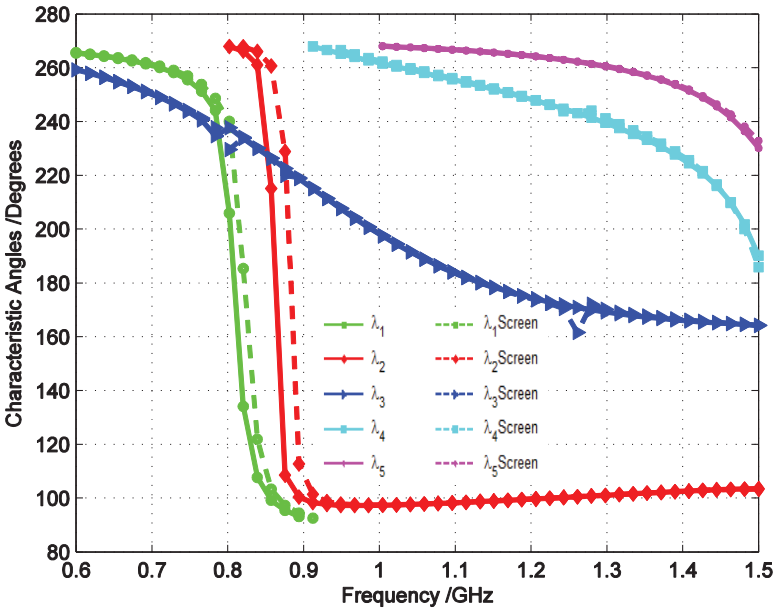

Figure 3-20. Characteristic angles of the characteristic modes for the cases of no components and the case with the addition of screen.

By visual inspection of the current distributions in Figure 3-21, there is very little changes in the current distributions of λ_1 with the addition of the screen. There is high current density on both the longer edges and the metal strips. Similar observations apply to the case of λ_2, with the exception that the regions of high current density is more balanced (similar in magnitude) on the opposite sides than those in λ_2. The trends between the current distributions and the E-field distributions in Figure 3-22 are similar to previous cases.

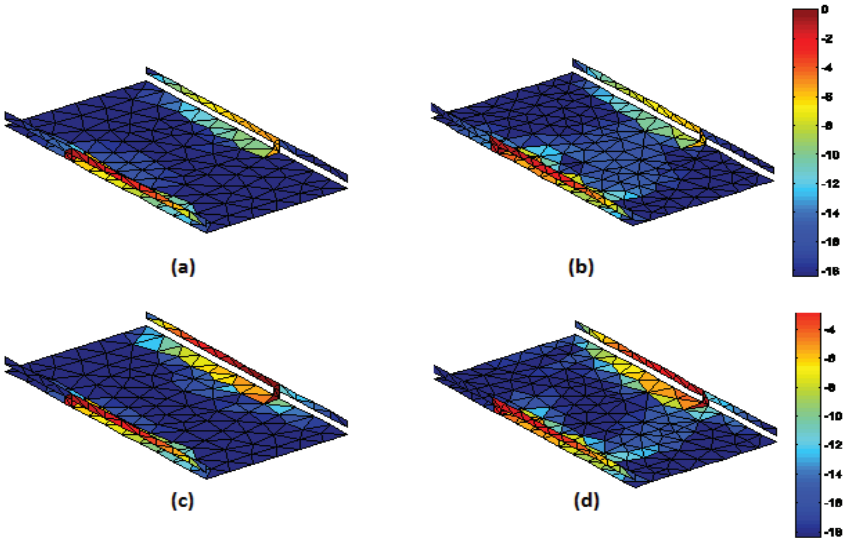

Figure 3-21. Current distributions for: (a) λ_1 - no components (b) λ_1 - screen (c) λ_2 - no components (d) λ_2 – screen.

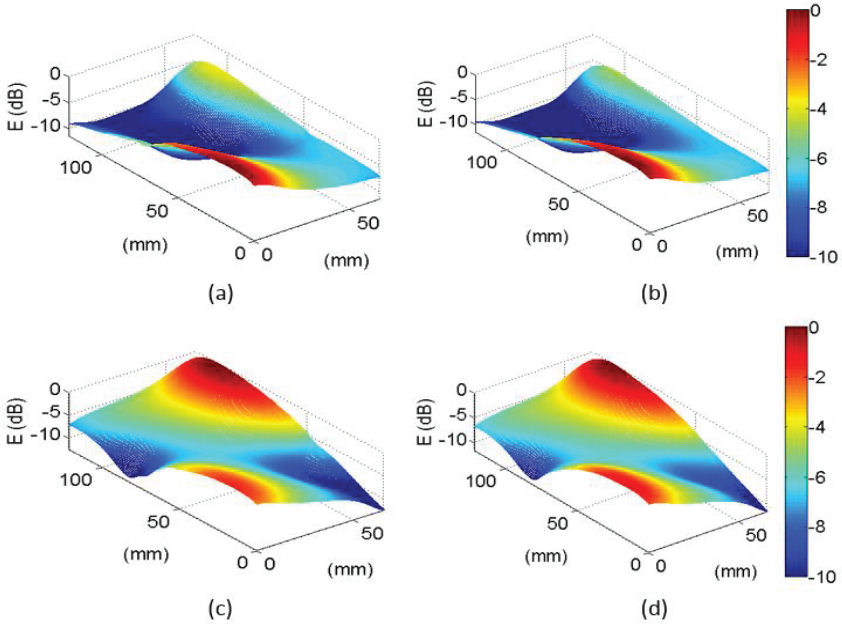

Figure 3-22. E-field distributions for: (a) λ_1 - no components (b) λ_1 - screen (c) λ_2 - no components (d) λ_2 - screen.

In Table 3-8, it is noted that in the near fields, the x- and z-components are more dominant in the E-field for both λ_1 and λ_2, whereas the z-component is more dominant in the H-field. The addition of the screen does not change the dominance of the components appreciably.

Table 3-8. Estimation of the dominant components for λ_1 and λ_2.

	E-field - no components	E-field - screen	H-field - no components	H-Field - screen
λ_1 x-component	0.5232	0.5276	0.2325	0.2222
λ_1 y-component	0.0350	0.0354	0.2359	0.2416
λ_1 z-component	0.4419	0.4370	0.5316	0.5362
λ_2 x-component	0.5501	0.5391	0.2351	0.2506
λ_2 y-component	0.0295	0.0287	0.1190	0.1214
λ_2 z-component	0.4204	0.4323	0.6459	0.6279

3.5 Combined Effects of all Components on the Characteristic Modes at Low Frequency

In a final analysis, we added all the components in the same way as described before and evaluated their combined effects on the characteristic modes. The combined effects of all the components caused more significant changes in the individual modes when compared to the effects by the individual components (see Figure 3-23 and Figure 3-24). First, λ_1 experienced a reduction in its resonant frequency from 805 MHz to 780 MHz, as opposed to an increase as recorded in the cases of the screen, microphone and battery. λ_2 had an increase similar to that of the battery case in that there was an increase in its resonant frequency. The most significant impact is experienced by λ_4. Its resonant frequency has decreased from beyond 1.5 GHz in all cases so far to around 1.35 GHz. However, since the new resonant frequency falls outside our range of interest (700 MHz to 1000 MHz), no further analysis was performed on λ_4.

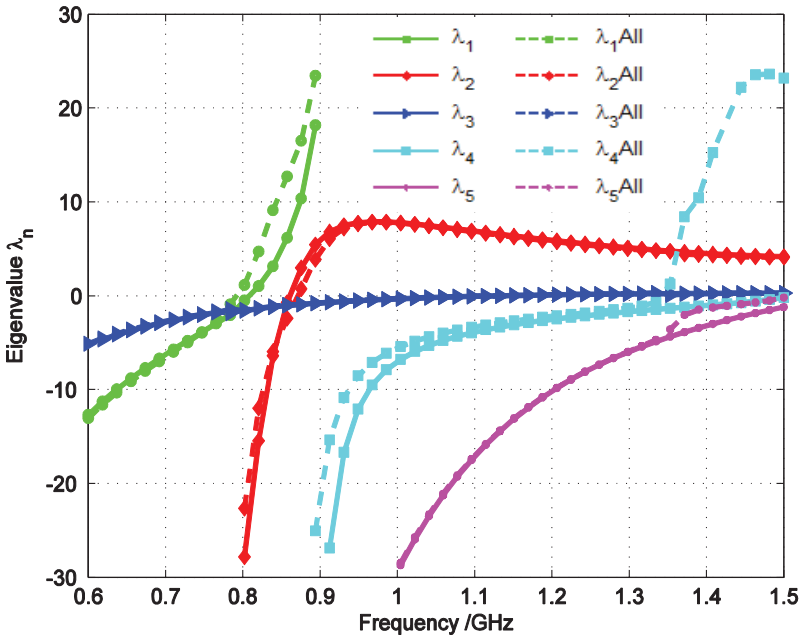

Figure 3-23. Eigenvalues of the characteristic modes for the cases of no components (strip loaded base structure) and the case with the addition of all components (denoted "All").

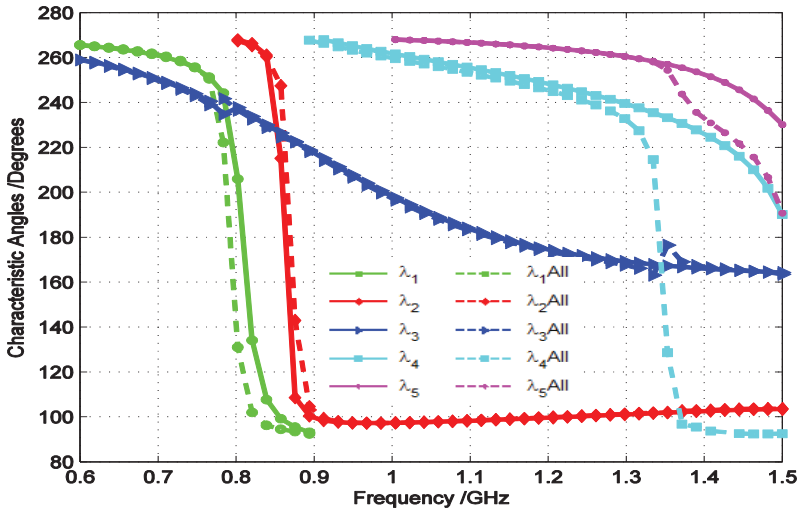

Figure 3-24. Characteristic angles of the modes for the cases of no components (strip loaded base structure) and the case with the addition of all components (denoted "All").

The sudden reduction in the resonant frequencies of λ_1 and λ_4 can be attributed to the increase in the electrical length of the whole structure as a result of the interaction between the individual components on the structure thereby causing the modes to resonate at lower frequencies.

Overall, there has been a relative increase in the frequency gap between the resonant frequencies of λ_1 and λ_2. Thus it has become impossible to excite the two modes simultaneously to form a broadband antenna. Simultaneous excitation of the two modes will now lead to the formation of two narrowband resonances. λ_1 and λ_2 were introduced as a result of the capacitance between the two metal strips. However, the introduction of the components, especially the battery, substantially disturbed the capacitance between the two strips.

Two ECC calculations were made to accommodate for the expansion of the frequency gap created between the two resonant values. The first was done at 900 MHz for λ_3 and at 850 MHz for λ_1 and λ_2 just as in the case of the strip-loaded base structure without any internal components. ECC values of 0.7514, 08223 and 0.9989 were obtained for λ_1, λ_2 and λ_3 respectively. This implies that there is significant change in the electromagnetic properties of λ_1 and λ_2 and therefore an entirely new analysis is required for feeding and excitation of those two modes. Another ECC analysis was carried out at 900 MHz for λ_2 and λ_3 and then at 800 MHz for λ_1. This is because the resonant frequency of λ_1 was reduced from 805 MHz to 780 MHz, whereas that of λ_2 was increased from 860 MHz to 880 MHz. ECC values 0.9338, 0.9335 and 0.9989 were recorded for λ_1, λ_2 and λ_3 respectively. Thus we can conclude that the shift in resonant frequency has caused a corresponding shift in the position of the eigenvalues.

Even though there is a significant change in the current distribution on λ_3, which is the fundamental mode, the principal current concentration on the metal strips remains the same. The E-field distribution shown in Figure 3-25 also confirms that there is a high possibility of still exciting it just as it was in [7].

The significant impact of the combined components is on λ_2 which had a relatively lower ECC value when compared to the other two modes. From the E-field distribution in Figure 3-26, it can be seen that some changes must be done to the structure to push the two modes together for single mode excitation of λ_1 and λ_2 to get broadband formation.

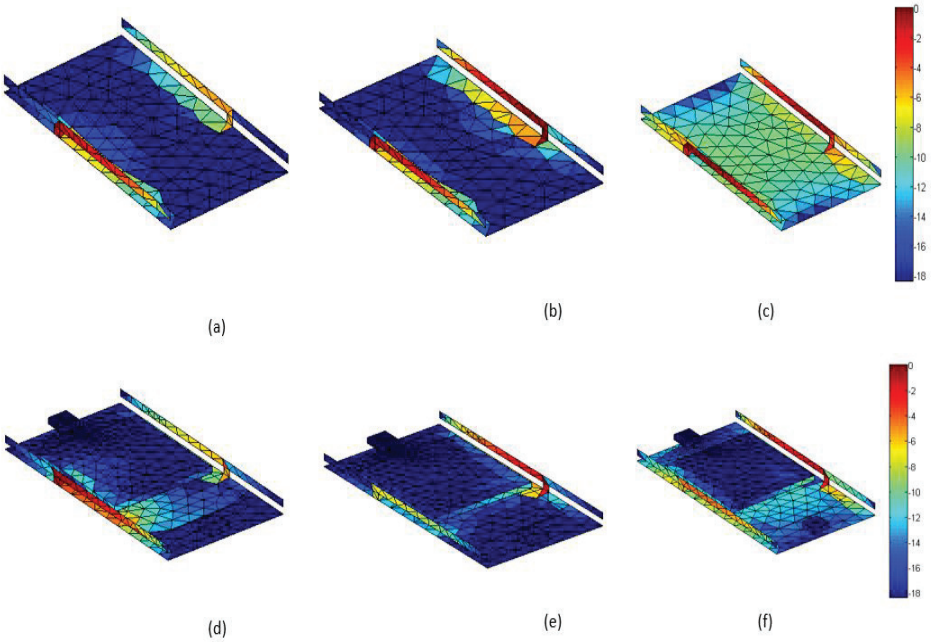

Figure 3-25. Current distributions for: (a) λ_1 - no components (b) λ_2 - no components (c) λ_3 - no components (d) λ_1 – all components (e) λ_2 – all components (f) λ_3 – all components.

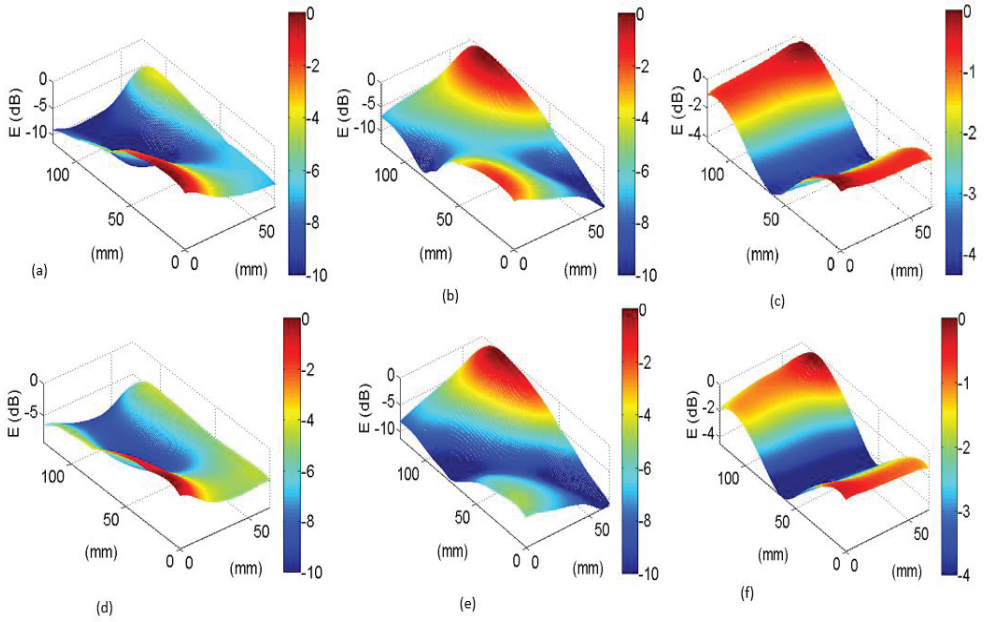

Figure 3-26. E-field magnitude distributions for: (a) λ_1 - no component (b) λ_2 - no component (c) λ_3 - no component (d) λ_1 – complete design (e) λ_2 – complete design (f) λ_3 - complete design.

Table 3-9. Estimation of the dominant components for the whole structure.

	E-field - no components	E-field - complete structure	H-field - no components	H-Field - complete structure
λ_1 x-component	0.5232	0.5276	0.2325	0.2222
λ_1 y-component	0.0350	0.0354	0.2359	0.2416
λ_1 z-component	0.4419	0.4370	0.5316	0.5362
λ_2 x-component	0.5501	0.5702	0.2351	0.2253
λ_2 y-component	0.0295	0.0662	0.1190	0.1152
λ_2 z-component	0.4204	0.3636	0.6459	0.6595
λ_3 x-component	0.0304	0.0340	0.9269	0.9228
λ_3 y-component	0.3033	0.3084	0.0071	0.0114
λ_3 z-component	0.6663	0.6578	0.0661	0.0658

3.6 Summary

1. The introduction of camera, microphone, screen and battery individually affects the resonant frequency of the two modes (λ_1 and λ_2) introduced by the shorting pins but maintains almost all the electric and magnetic properties with ECC greater than 0.9.

2. λ_3 which was as a result of the base structure is unaffected by the individual components as it always maintained ECC greater than 0.99.

3. The combined effect of all the components increased the electrical length of the entire structure thereby reducing the resonant frequency of λ_1 which was introduced as a result of the capacitance between the two shorting pins.

4. The structure must be modified to push the two modes λ_1 and λ_2 together for single excitation of the two modes to cause broadband performance.

CHAPTER 4

4 Effects of Internal Components on Characteristic Modes at High Frequency

In this chapter, the effect of the internal components on the characteristic modes was analyzed at high frequency at 1.8 GHz in a frequency range from 1.6 GHz to 2.3 GHz.

4.1 Effects of the Camera on the Characteristic Modes at High Frequency

The first component to be analyzed was the camera. As before, the characteristic eigenvalues and characteristic angles before and after the addition of camera are plotted (see Figure 4-1 and Figure 4-2). For the high frequency case, the first 6 modes with eigenvalues having the magnitudes of less than 6 were analyzed. The numbering order of the modes in the high frequency is independent of the order in the low frequency case.

Unlike the low frequency case that saw a significant change in the resonant frequency of some of the modes due to the introduction of the camera, there is no visible change in the resonant frequencies of the characteristic modes. This could be due to the component being added in a region where the currents and near fields of these modes are relative low, which resulted in minimal disturbance of the modes.

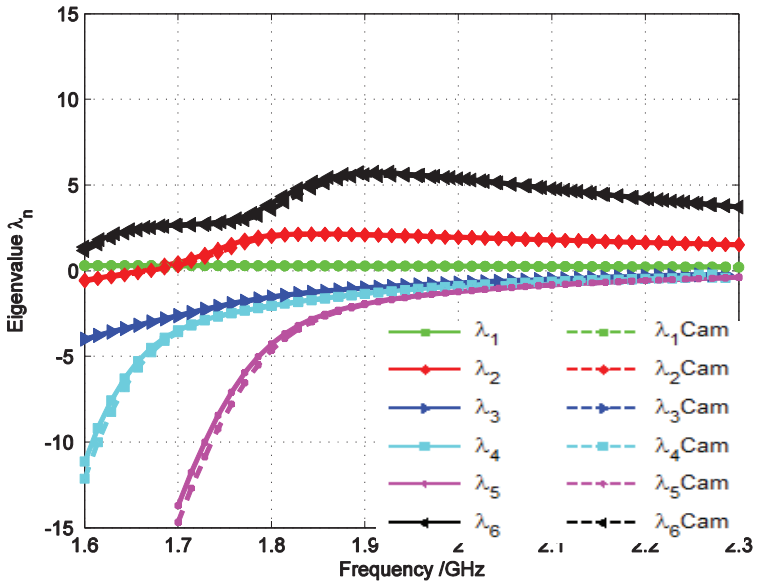

Figure 4-1. Eigenvalues of characteristic modes for the case of no components (strip loaded base structure) and the case with the addition of camera (denoted "Cam").

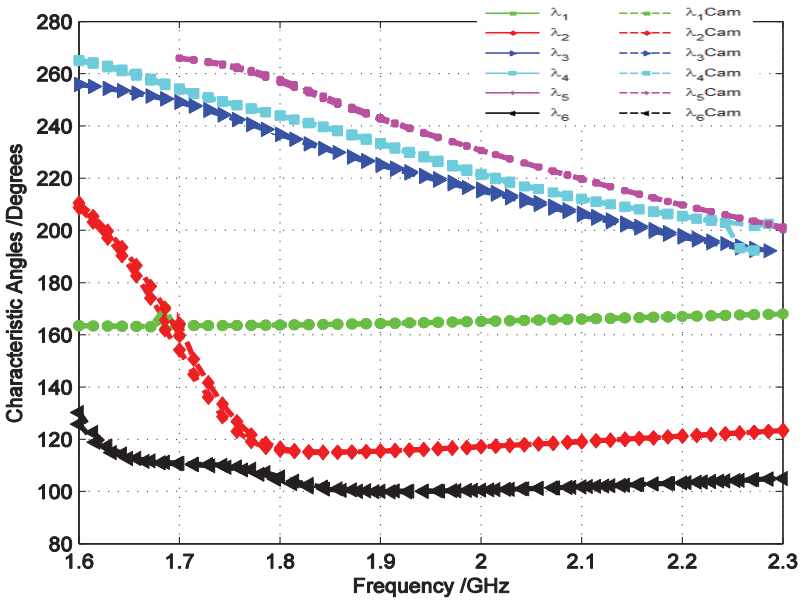

Figure 4-2. Characteristic angles of the modes for the case of no components (strip loaded base structure) and the case with the addition of camera (denoted "Cam")

Table 4-1. ECCs of eigenvalues for the addition of camera for high frequency

Characteristic modes	ECC
λ_1	1
λ_2	0.9903
λ_3	0.9996
λ_4	0.9979
λ_5	0.9950
λ_6	0.9869

The ECC values of Table 4-1 show that there is a minimal, if not negligible, impact on the characteristic mode properties as a result of the introduction of the camera at the high frequency. Just as it was shown in the case of the low frequency, ECC values of 0.9 or more imply that almost all the electromagnetic properties are maintained at a particular frequency and therefore no further analysis was needed.

With all the modes having ECC of above 0.99, we examined the correlation between individual modes in the same structure. For MIMO operation, ECC values of 0.5 or smaller is considered adequate as it implies minimum correlation between two incoming signals and thus high data throughput [1]. In TCM, ECC between different modes in the same structure should be 0, since the characteristic modes are orthogonal by definition. From Table 4-2, it can be seen that all ECC values between two different modes are approximately zero. Thus it is confirmed that it is possible to excite one mode and not have any influence from other modes inherent in the same structure.

Table 4-2. ECCs values for eigenvalues within the same camera structure

	λ_1	λ_2	λ_3	λ_4	λ_5	λ_6
λ_1	1	0.002	0.00024	0.00002	0.00019	0.00026
λ_2	0.002	1	0.00054	0.00039	0.0006	0.00052
λ_3	0.00024	0.00054	1	0.000081	0.00001	0.000049
λ_4	0.00002	0.00039	0.000081	1	0.00043	0.00038
λ_5	0.00019	0.0006	0.00001	0.00043	1	0.0042
λ_6	0.00026	0.00052	0.000049	0.00038	0.0042	1

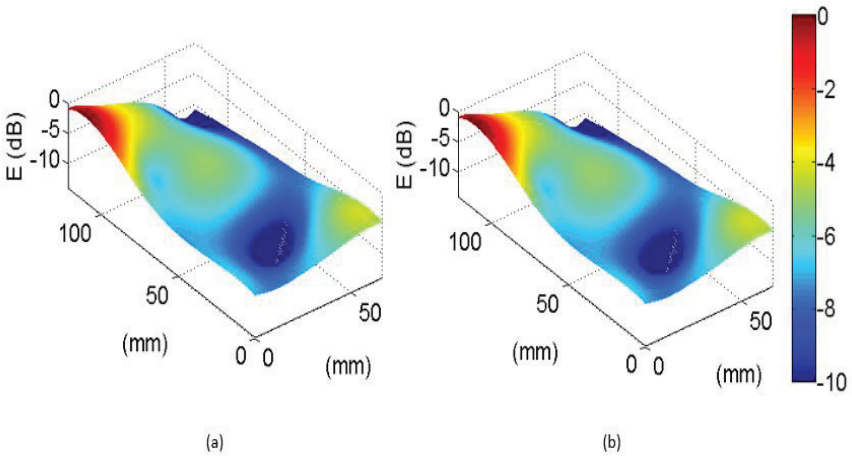

Figure 4-3. E-field distribution for camera and complete structure at high frequency.

4.2 Effects of the Microphone on the Characteristic Modes at High Frequency

The previous analysis was repeated for the case of the microphone, and the results are provided below.

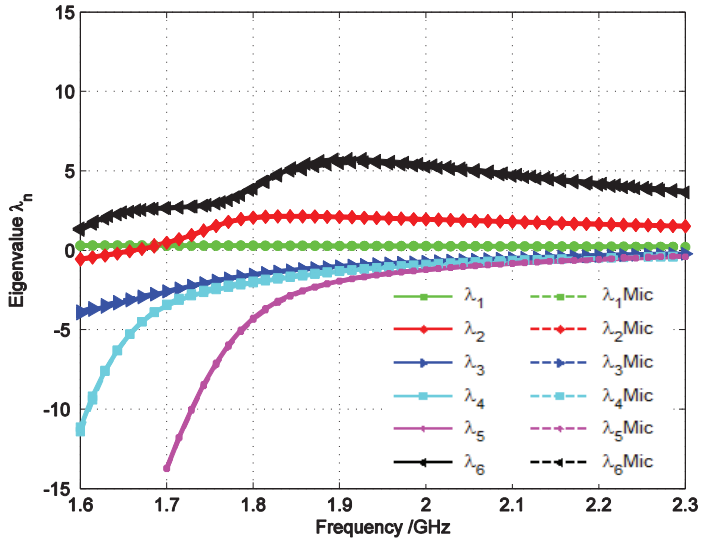

Figure 4-4. Eigenvalues of the characteristic modes for the case of no components (strip loaded base structure) and the case with the addition of microphone (denoted "Mic") at high frequency.

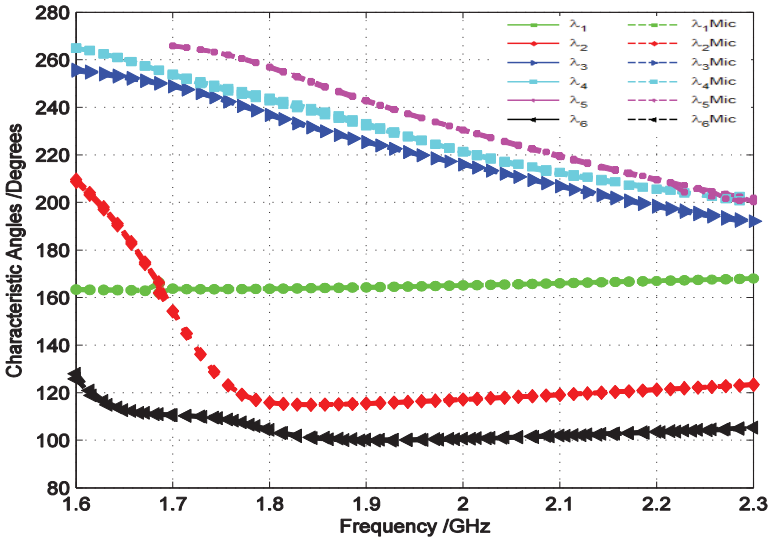

Figure 4-5. Characteristic angles of the modes for the case of no components (strip loaded base structure) and the case with the addition of microphone (denoted "Mic") at high frequency.

Table 4-3. ECCs of eigenvalues for the addition of microphone for high frequency

Characteristic modes	ECC
λ_1	0.9999
λ_2	0.9903
λ_3	0.9998
λ_4	0.9993
λ_5	0.9998
λ_6	0.9996

As can be seen in Table 4-3, with ECC values all greater than 0.99 (almost 1), we can confidently conclude that the microphone had no impact on these characteristic modes.

As can be seen in Table 4-4, the ECC between individual modes within the structure with microphone is approximately zero (and ideally exactly zero), hence there is perfect orthogonality between the modes in the structure. This implies the excitation of one mode will not in any way interfere with the other modes.

Table 4-4. ECCs values for eigenvalues within the same microphone structure

	λ_1	λ_2	λ_3	λ_4	λ_5	λ_6
λ_1	1	0.002	0.00024	0.00003	0.00016	0.00017
λ_2	0.002	1	0.00052	0.00004	0.00037	0.0005
λ_3	0.00024	0.00052	1	0.00007	0.00008	0.00007
λ_4	0.00003	0.00004	0.00007	1	0.0003	0.0004
λ_5	0.000016	0.00037	0.00008	0.0003	1	0.0039
λ_6	0.000017	0.0005	0.00007	0.0004	0.0039	1

4.3 Effects of the Screen on the Characteristic Modes at High Frequency

The previous analysis was repeated for the case of the screen, and the results are provided below.

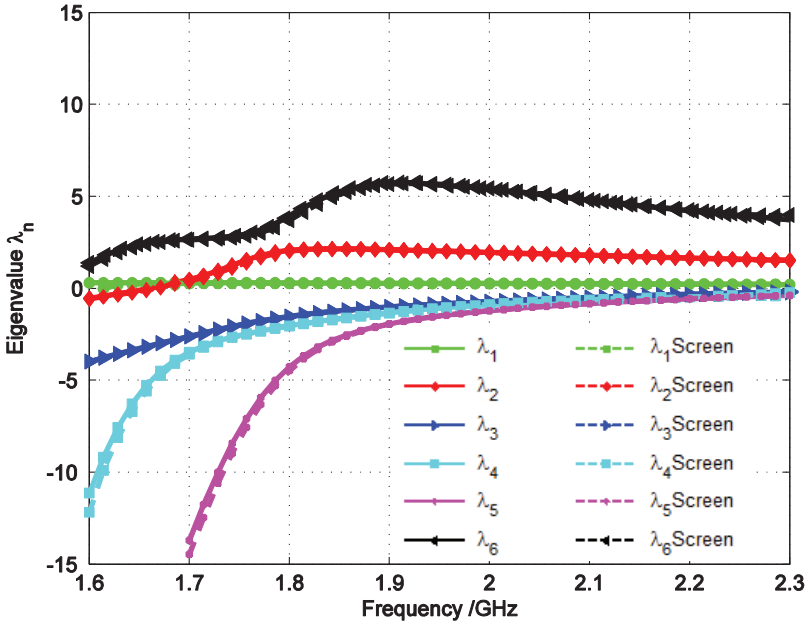

Figure 4-6: Eigenvalues of the characteristic modes for the case of no components (strip loaded base structure) and the case with the addition of screen at high frequency

Table 4-5. ECCs of eigenvalues for the addition of screen for high frequency

Characteristic modes	ECC
λ_1	1
λ_2	0.9961
λ_3	0.9988
λ_4	0.9982
λ_5	0.9968
λ_6	0.9941

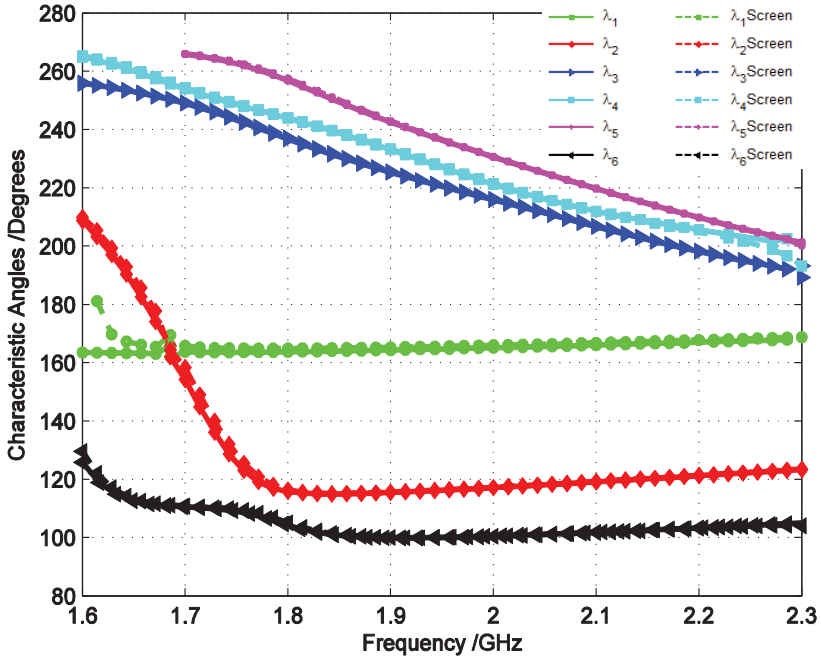

Figure 4-7. Characteristic angles of the modes for the case of no components (strip loaded base structure) and the case with the addition of screen at high frequency.

Like the previous case, the ECC for individual modes when compared to the other modes within the same structure is approximately 0 (see Table 4-6).

Table 4-6. ECCs values for eigenvalues within the same screen structure

	λ_1	λ_2	λ_3	λ_4	λ_5	λ_6
λ_1	1	0.002	0.00024	0.00002	0.0002	0.00025
λ_2	0.002	1	0.00054	0.00037	0.00052	0.00056
λ_3	0.00024	0.00054	1	0.00009	0.0001	0.00004
λ_4	0.00002	0.00037	0.00009	1	0.00034	0.00032
λ_5	0.0002	0.00052	0.00004	0.00034	1	0.0013
λ_6	0.00025	0.00056	0.00032	0.00032	0.0013	1

4.4 Effects of the Battery on the Characteristic Modes at High Frequency

The previous analysis was repeated for the case of the battery, and the results are provided below.

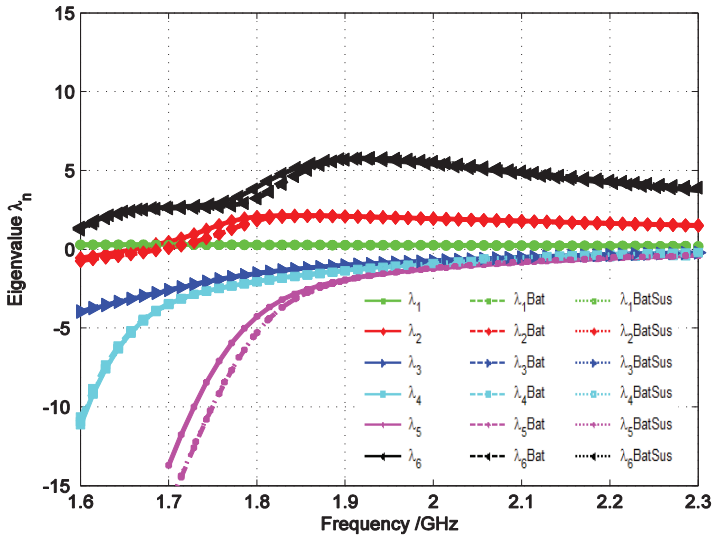

Figure 4-8. Eigenvalues of the characteristic modes for the cases of no components and the addition of battery ("Bat" denotes battery attached to ground plane, "BatSus" denotes battery suspended above ground plane) at high frequency.

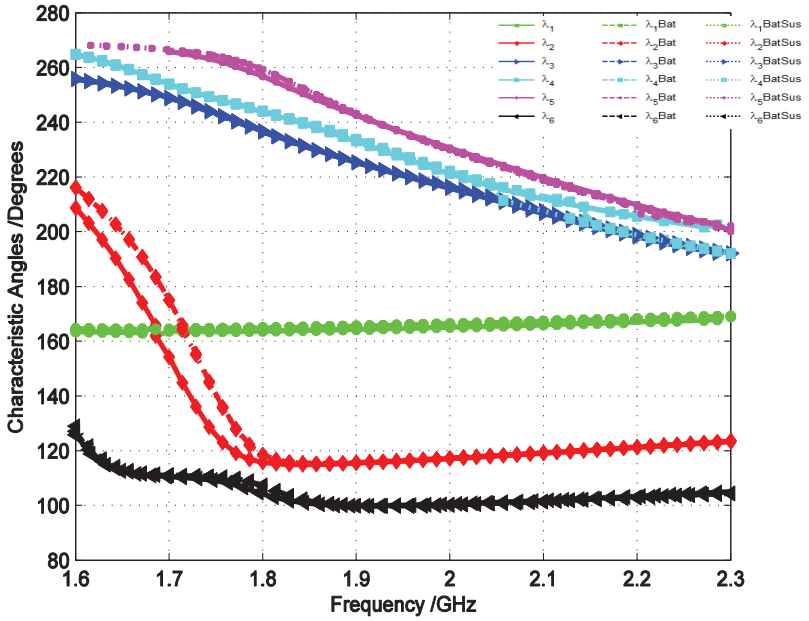

Figure 4-9. Characteristic angles of the modes for the cases of no components and the addition of battery ("Bat" denotes battery shorted/connected to ground plane, "BatSus" denotes battery suspended above ground plane) at high frequency.

At high frequency, the gap between the battery and the strip-loaded base structure introduces more capacitance into the entire structure. This shown by the reduction in the eigenvalues of λ_2 and λ_6 which were positive and hence inductive. Also the eigenvalue of λ_5 which was negative (capacitive) experiences a relative increase in the magnitude of eigenvalue.

Table 4-7. ECCs of eigenvalues for the addition of battery for high frequency

Characteristic modes	Battery connected via shorting pin	Battery suspended
λ_1	0.9995	0.9994
λ_2	0.9360	0.9402
λ_3	0.9992	0.9986
λ_4	0.9861	0.9868
λ_5	0.9698	0.9710
λ_6	0.9063	0.9114

Table 4-8. ECCs values for eigenvalues within the same battery connected via shorting pin structure

	λ_1	λ_2	λ_3	λ_4	λ_5	λ_6
λ_1	1	0.0019	0.00023	0.00002	0.00024	0.0005
λ_2	0.0019	1	0.00027	0.00055	0.00057	0.00044
λ_3	0.00023	0.00027	1	0.00004	0.0000075	0.000077
λ_4	0.00002	0.00055	0.00004	1	0.000047	0.000026
λ_5	0.00024	0.00057	0.0000075	0.000047	1	0.0014
λ_6	0.0005	0.00044	0.000077	0.000026	0.0014	1

Table 4-9. ECCs values for eigenvalues within the same battery suspended structure

	λ_1	λ_2	λ_3	λ_4	λ_5	λ_6
λ_1	1	0.0019	0.00023	0.00002	0.00027	0.0005
λ_2	0.0019	1	0.00027	0.00053	0.00056	0.00044
λ_3	0.00023	0.00027	1	0.00004	0.00001	0.000077
λ_4	0.00002	0.00053	0.00004	1	0.000052	0.000026
λ_5	0.00027	0.00056	0.00001	0.000052	1	0.0012
λ_6	0.0005	0.00044	0.000077	0.000026	0.0012	1

Table 4-10 and Table 4-9 show the ECC values between the modes in the case of battery suspended and the case of battery connected via shorting pin. In both cases there exist perfect orthogonality between the modes.

4.5 Combined Effects of all Components on the Characteristic Modes at High Frequency

The previous analysis was repeated for the case of all components, and the results are provided below.

With all individual components giving ECC values of greater than 0.9 (before and after adding of each component), we focused our attention on the effect of all components on the characteristic modes of the strip loaded base structure. Here, we used the shorted battery design as it is closer to real life implementation than the suspended battery design.

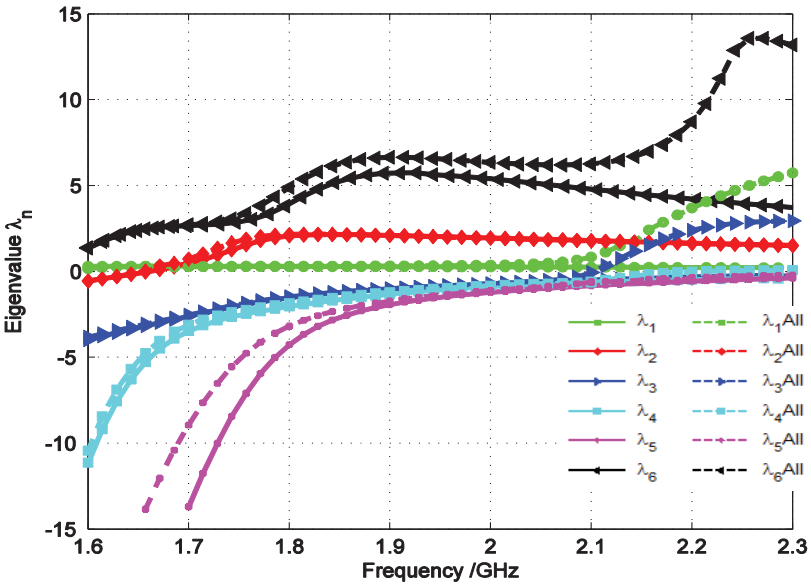

Figure 4-10. Eigenvalues of the characteristic modes for the cases of no components (strip loaded base structure) and the case with the addition of all components (denoted "All") at high frequency

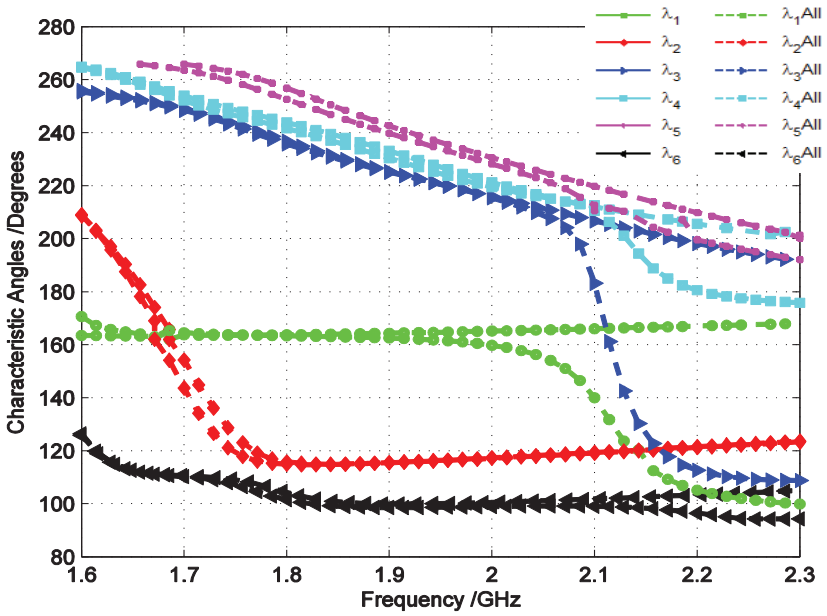

Figure 4-11. Characteristic angles of the modes for the cases of no components (strip loaded base structure) and the case with the addition of all components (denoted "All") at high frequency.

Just as in the case of the low frequency, the many added components increased the electrical length of the strip-loaded base structure, thus reducing the resonant frequency of λ_3. The eigenvalue λ_5 reduces (less capacitive) and λ_6 which initially is positive increases (become more inductive). Thus we can say that at the high frequency, the entire structure became more inductive and λ_5 had an ECC value less than 0.9, thus a new analysis needed.

Table 4-11. ECCs of eigenvalues for the complete structure for the high frequency

Characteristic modes	ECC
λ_1	0.9993
λ_2	0.9732
λ_3	0.9535
λ_4	0.9318
λ_5	0.8729
λ_6	0.9213

Table 4-12. ECCs values for eigenvalues within the same complete structure

	λ_1	λ_2	λ_3	λ_4	λ_5	λ_6
λ_1	1	0.002	0.00014	0.000177	0.000209	0.000223
λ_2	0.002	1	0.00023	0.00018	0.000097	0.00043
λ_3	0.00014	0.00023	1	0.000011	0.000011	0.000009
λ_4	0.000177	0.00018	0.000011	1	0.000078	0.00011
λ_5	0.000209	0.000097	0.000011	0.000078	1	0.00063
λ_6	0.000223	0.00043	0.000009	0.00011	0.00063	1

In Figure 4-12, some key differences in the current density can be observed on the right strip. There is higher current in the case of the complete design. From Biot-Savart Law, the magnetic field intensity is proportional to the current density in a metal strip. Thus the presence of the higher current leads to a higher magnetic field around the entire structure as shown in Figure 4-13(d).

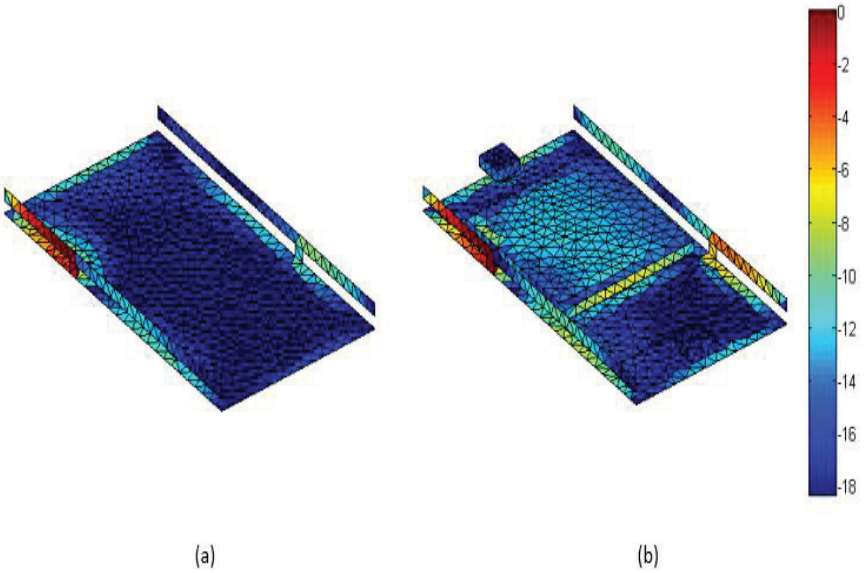

Figure 4-12. Current distributions for: (a) λ_5 in the case of no component. (b) λ_5 in the case complete design.

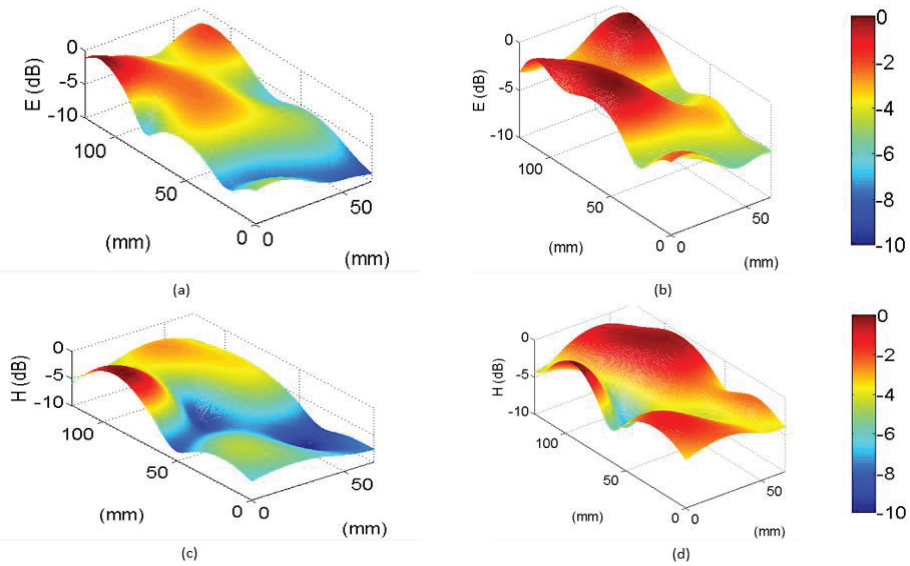

Figure 4-13. E-field distributions for: (a) λ_5 - no component (b) λ_5 - Complete design H-field distributions for (c) λ_5 – no component (d) λ_5 – Complete design

Table 4-13 Estimation of the dominant components for E and H fields of λ_5 of the complete design

	E-Field		H-Field	
Direction	No components	Complete design	No components	Complete design
x-component	0.3731	0.2915	0.2929	0.4011
y-component	0.0898	0.1337	0.3271	0.3889
z-component	0.5370	0.5749	0.3801	0.2100

As can be seen in Table 4-12, even though the dominant component in the E-field is maintained in the z direction, the dominant component in the H-field has been altered from the z to the x component. This can affect the feeding and/or the simultaneous excitation of more than one mode to achieve broadband and multiband operation.

Further analysis of λ_5 will be made in the next chapter during the correction (or turning) of the entire structure to mitigate the increased resonant frequency gap between λ_1 and λ_2 in the low frequency case.

CHAPTER 5

5 Tuning of Characteristic Modes for Antenna Design with Components by Varying Capacitance

As described in Chapter 3, the introduction of all internal components caused a further separation of the resonance frequencies of two characteristic modes in the low frequency. This prevented the simultaneous excitation of the two modes to form a broadband resonance. In this chapter, the aim is to restore the modes to their original resonant frequencies or close the gap between the two resonant frequencies to achieve a broadband resonance at the low frequency.

A closer look at the current distribution figures in Chapters 3 and 4 (i.e., Figure 3-25 and Figure 4-5) revealed that the low frequency case leads to high current density on the longer arms of the capacitive strips whereas the high frequency case shows similar effect on the shorter arm of the strips. In view of this, the longer strip arm was altered to influence the characteristc modes at the low frequency case, leaving the shorter arm intact. The width of the longer arm of the capacitve strips was reduced by 1.5 mm, leaving the overall height of 7 mm from the ground plane unchanged. In effect, this caused an increase in the air gap between the capacitive strips and the ground plane, thereby reducing the capacitance between the two conductors.

5.1 Low Frequency Analysis after Varying Capacitance

Maintaining the capacitive strip length and decreasing the capacitance between the strip and the ground plane have caused the two modes (λ_1 and λ_2) to resonate closer to each other (Figure 5-1). The resonant frequency of λ_1 has increased from 790 MHz to 810 MHz whereas that of λ_2 has decreased by about 5 MHz (from 865 MHz to 860 MHz). The gap between the resonant

frequencies of the two modes are now about 50 MHz, as compared to about 75 MHz before the strip width modification.

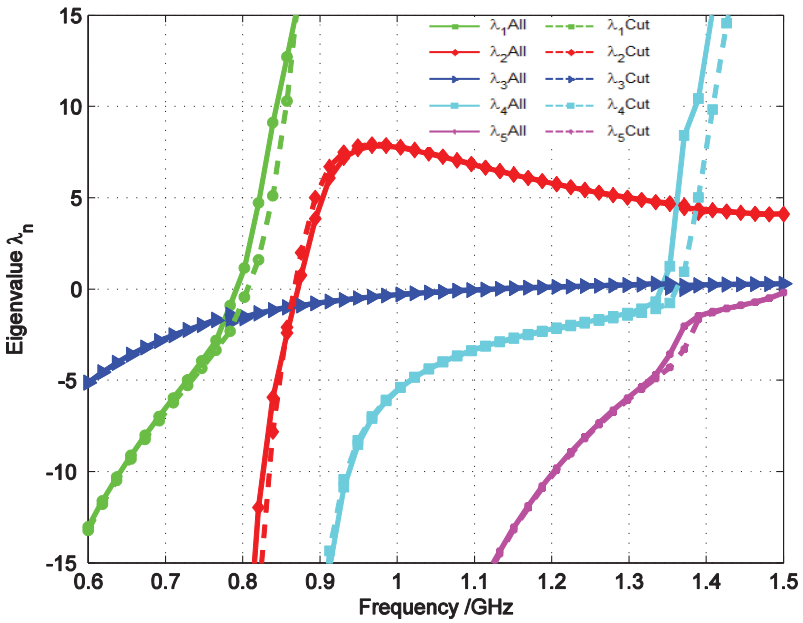

Figure 5-1. Eigenvalues of the characteristic modes for the cases of all components (denoted "All") and the case after varying capacitance (denoted "Cut") at low frequency.

Table 5-1 summarizes the ECC values for the cases before and after decreasing the capacitance between the longer arms and the ground plane. In each case they were compared to the case of no components. In the final column the ECC values were obtained by correlating the far field patterns in the two cases of the complete structure with components, where they only differ by the width of the longer arm of the capacitance strips. In all instances, the ECC values are greater in the case of decreasing the capacitance than the case before. Thus it can concluded altering the capacitance provides a good means of shifting around the resonant frequency of a characteristic mode without causing lot of changes to its electromagnetic properties.

Table 5-1. ECC before and after decreasing capacitance and also for full design for the low frequency

Characteristic modes	ECC (before decreasing capacitance)	ECC (after decreasing capacitance)	ECC (full design and full design with altered strips)
λ_1	0.9338	0.9544	0.9067
λ_2	0.9335	0.9688	0.9613
λ_3	0.9989	0.9996	0.9997

The current distributions of the first three characteristic modes before and after the strip modification are shown in Figure 5-2. The corresponding graph for the near field E-field distributions are shown in Figure 5-3.

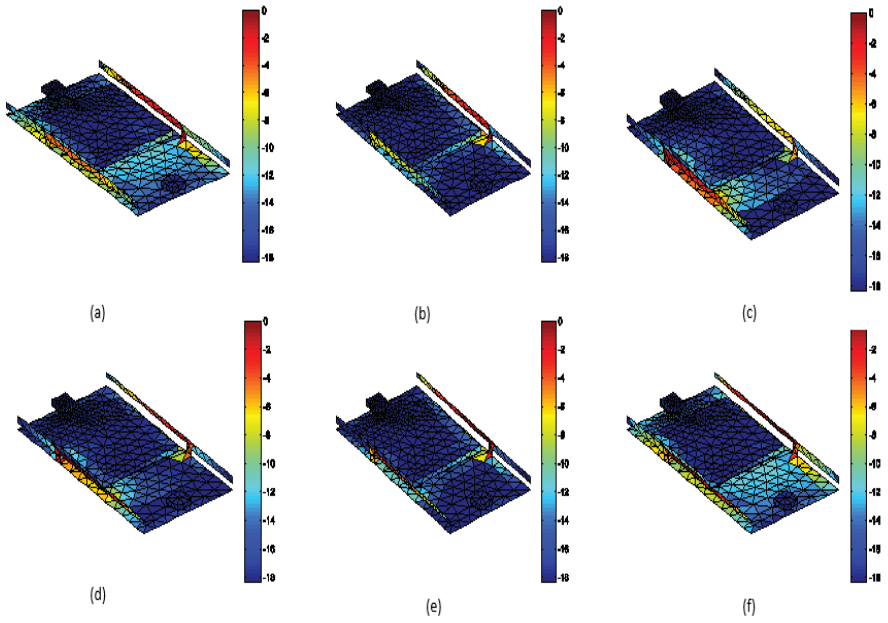

Figure 5-2. Current distributions for: (a) λ_1 – complete design (b) λ_2 – complete design (c) λ_3 – complete design (d) λ_1 – complete design (after varying capacitance) (e) λ_2 – complete design (after varying capacitance) (f) λ_3 – complete design (after varying capacitance)

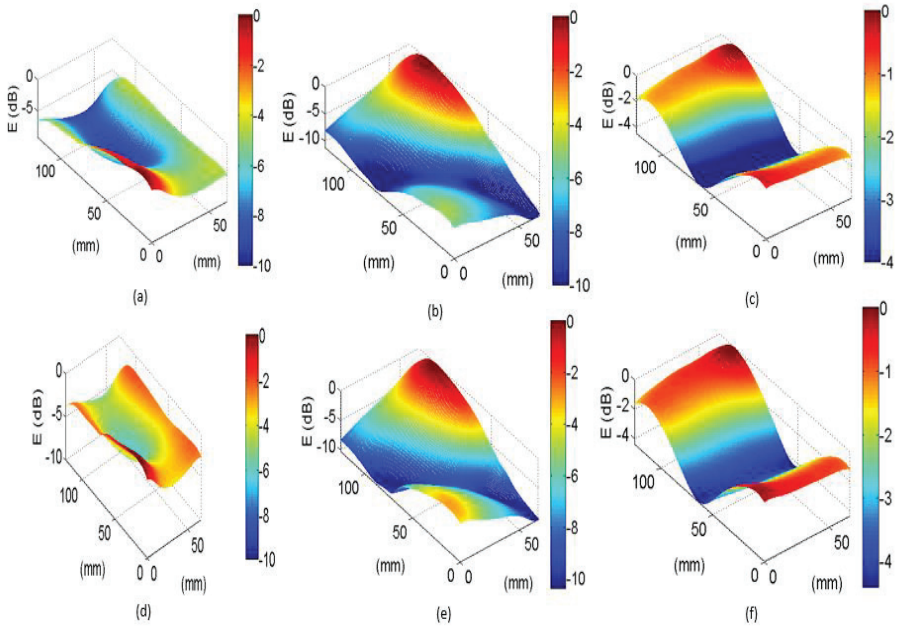

Figure 5-3. E-field magnitude distribution for: (a) λ_1 – complete design (b) λ_2 – complete design (c) λ_3 – complete design (d) λ_1 – complete design (after varying capacitance) (e) λ_2 – Complete design (after varying capacitance) (f) λ_3 – complete design (after varying capacitance)

From Figure 5-2, it can be observed that a relatively higher current density resides on both arms of the capacitance strips in the case of the narrower longer arms as compared to the case of the original longer arm (before altering capacitance). This is largely due to the fact that the surface areas of the strips were reduced and for that matter had a relatively higher current density as compared to the initial case of wider capacitance strips.

In Figure 5-4, Figure 5-5 and Figure 5-6, we compare the 2D cuts of the far field pattern for each of the first three eigenmodes at the low frequency. The far field pattern of the fundamental mode shown in Figure 5-6 maintains its gain and directivity with little or no changes.

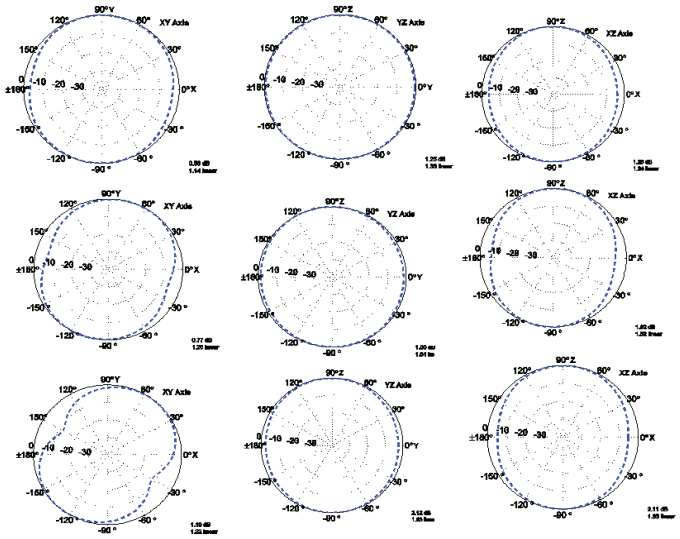

Figure 5-4. Far field pattern of λ_1 in 2D cuts: (a) xy-plane - no component (b) xz-plane - no component (c) yz-plane - no component (d) xy-plane - complete design (e) xz-plane - complete design (f) yz-plane - complete design (g) xy-plane - complete design (after cut) (h) xy-plane - complete design (after cut) (i) yz-plane - complete design (after cut)

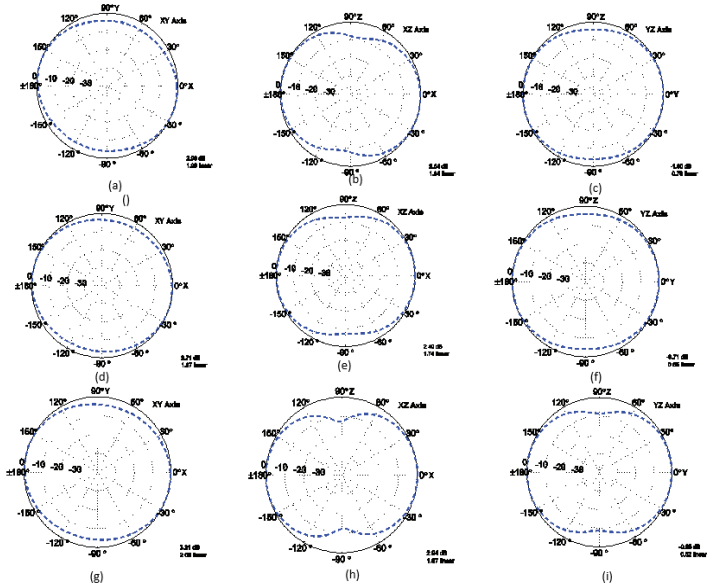

Figure 5-5. Far field pattern of λ_2 in 2D cuts: (a) xy-plane - no component (b) xz-plane - no component (c) yz-plane - no component (d) xy-plane - complete design (e) xz-plane - complete design (f) yz-plane - complete design (g) xy-plane - complete design (after cut) (h) xy-plane - complete design (after cut) (i) yz-plane - complete design (after cut)

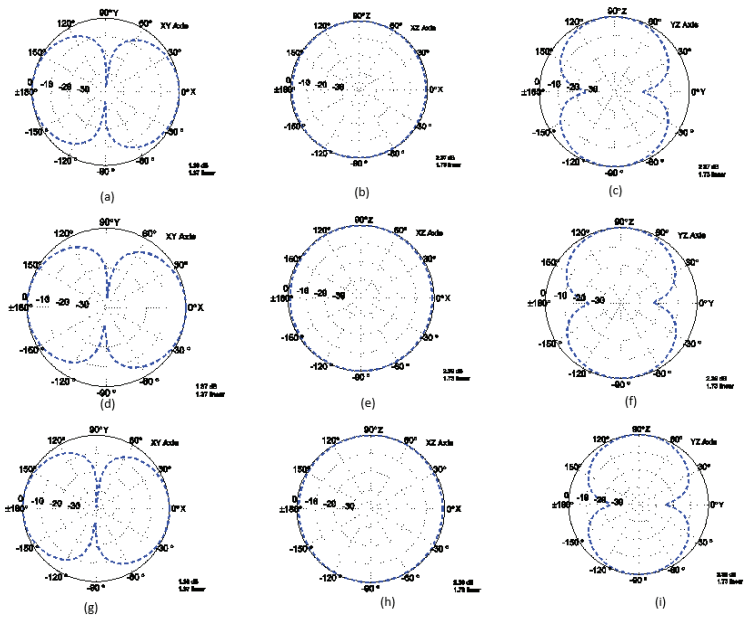

Figure 5-6. Far field pattern of λ_3 in 2D cuts: (a) xy-plane - no component (b) xz-plane - no component (c) yz-plane - no component (d) xy-plane - complete design (e) xz-plane - complete design (f) yz-plane - complete design (g) xy-plane - complete design (after cut) (h) xy-plane - complete design (after cut) (i) yz-plane - complete design (after cut)

5.2 High Frequency Analysis after Varying Capacitance

Apart from tuning the characteristic mode resonances at the low frequency, it is important to ensure that the tuning does not disturb the high frequency performance. Figure 5-7 show the eigenvalues of the characteristic modes before and after the capacitive strip modification.

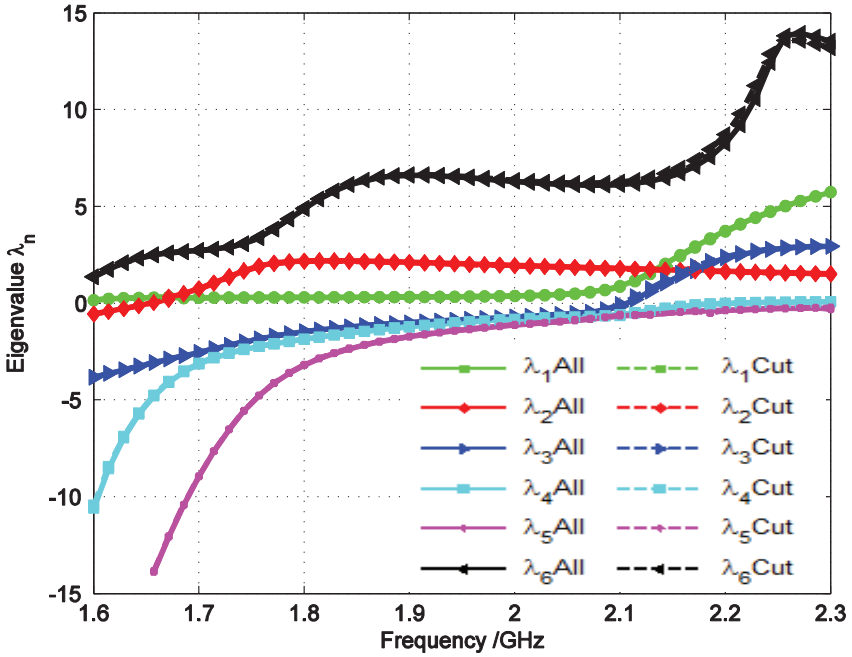

Figure 5-7. Eigenvalues of the characteristic modes for the cases of all components (denoted "All") and the case after varying capacitance (denoted "Cut") at high frequency.

Table 5-2. ECC before and after decreasing capacitance and also for full design for the high frequency

	ECC (before decreasing capacitance)	ECC (After decreasing capacitance)	ECC (full design and full design with altered strips)
λ_1	0.9993	0.9993	1
λ_2	0.9722	0.9722	1
λ_3	0.9554	0.9554	1
λ_4	0.9327	0.9327	0.9999
λ_5	0.8737	0.8737	0.9999
λ_6	0.9228	0.9228	0.9998

Table 5-2 contains similar information as in the Table 5-1 except in this case the analysis is for the high frequency cases. Two important points from Table 5-2 are the values in columns two and three are the same. Also, all the ECC values for column four are 1 or almost equal to 1. In the fourth column the ECC values were computed by correlating the far fields of each of the mode

in the case of no change in the capacitive strip with their corresponding modes in the case of width altered strips. The lack of impact of width alteration can be explained by the longer arms of the capacitive strips having minimal current density for the modes of interest at high frequency. Thus, in general, the shape of a structure can be changed at the minimum current density region(s) of a characteristic mode without significantly influencing the electromagnetic properties of that particular mode.

In a similar manner, altering the capacitance between the shorter arms of the capacitive strips will instead affect the resonant frequency for the high frequency case without having any major effects for the low frequency case. This is due to the fact that in Figure 4-12, there is higher current density on the shorter arms of the strips in the high frequency case, but minimal current density on the longer arms.

CHAPTER 6

6 Antenna Simulations

This chapter focuses on full-wave antenna simulations carried out with CST and the results are compared with those obtained from the study of characteristic modes with Matlab in Chapter 5. The full-wave CST simulations were performed using the Frequency Domain Solver for both the low and high frequencies, as described in the sections below.

6.1 Simulations at Low Frequency

Several methods are available for designing antennas that excite the chassis (e.g., [15]). However, the focus of the simulations was on the "T-strip" antenna (The strips with the shorting pin look like the letter "T"), which relied solely on characteristic mode analysis for its design [7].

The first objective was to obtain enough bandwidth from the original strip-loaded structure without altering the capacitive strip width explained in the previous chapter. Several simulations were carried out by varying the position of the feed point on one strip while keeping the other strip unchanged. The feed position is defined with respect to the distance from the center of the longer edge as shown in Figure 6-1 (note however that the figure shows the modification strip width in the longer arms, instead of the original strip width).

Two impedance matching software were employed in the simulation. The first was the in-built tuning feature in CST. This is primarily used to maximize the bandwidth. The second software, BetaMatch [16], gives matching component parameters for an optimum bandwidth and maximum power received by the antenna for transmission. The primary focus of the matching circuits used was to obtain as much bandwidth as possible. A sample of the tuning circuits used is shown in Figure 6-2.

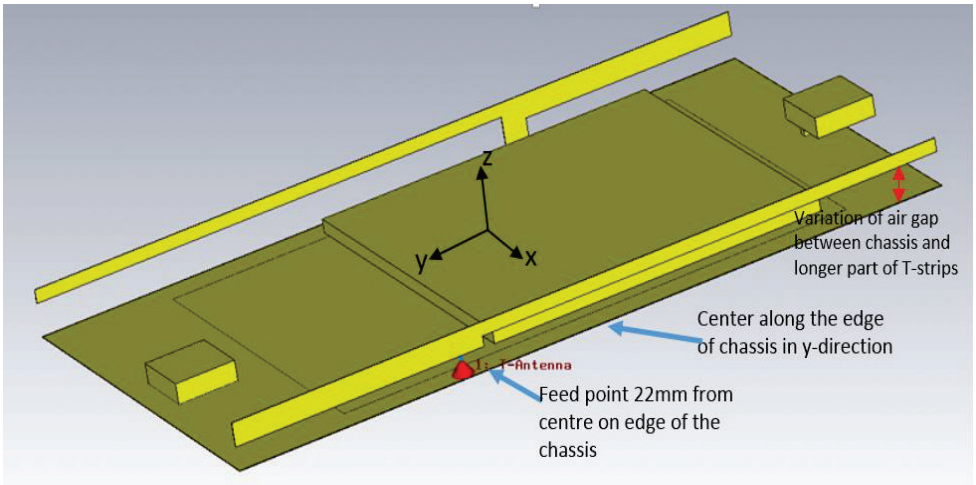

Figure 6-1. Final simulated T-strip antenna.

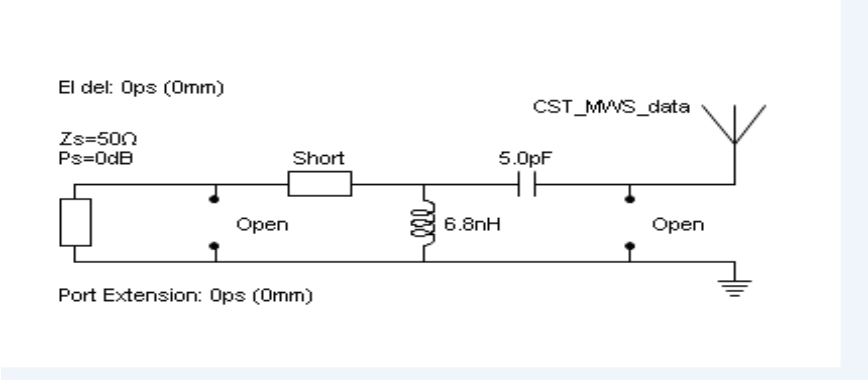

Figure 6-2. Sample tuning circuit in BetaMatch.

The results from the parametric study of the feed position are shown in Table 6-1. In Figure 6-3, the scattering (S) parameters for two of the feed points that gave an approximate bandwidth of 40 MHz.

Figure 6-3 shows that the two unmatched cases give two narrow-band resonances. One of the resonance is centered at 810 MHz for both cases which is same as the resonant frequency for λ_1 in Figure 5-1. The other resonance is centered at around 860 MHz for the 16 mm unmatched case which is the resonant frequency for λ_2 in Figure 5-1. In the 22 mm unmatched case, about the larger shift in the feed position caused the frequency gap between the two resonances to reduce.

Table 6-1. Bandwidth (BW) for different feed positions

Feed Position [mm]	Start Frequency [MHz]	End Frequency [MHz]	Bandwidth [MHz]
16	825.6	868.4	42.8
18	828.0	867.2	39.2
19	826.0	864.0	38
20	829.2	867.2	38
22	824.4	860.4	36
24	832.0	870.0	38
26	835.2	872.8	37.6
28	848.8	864.8	16

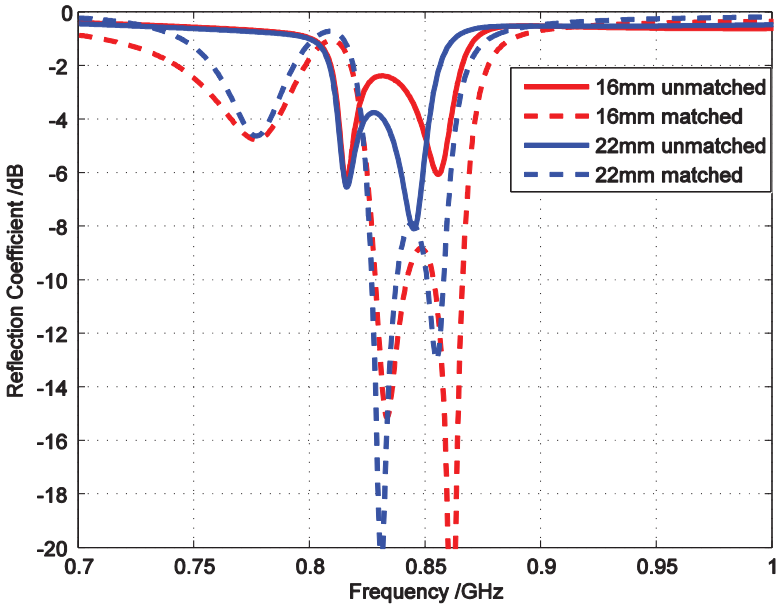

Figure 6-3. S-parameters for the low frequency for both matched and unmatched case at 16 mm and 22 mm

In the second set of simulations, the feed position was maintained at 22 mm, to be consistent to the case in [7]. We then increased the capacitance gap between the longer end of the strips and the chassis in multiples of 0.5 mm from 0 to 2.5 mm. In the previous chapter, the capacitance gap was employed to alter the resonant frequencies of the two modes (λ_1 and λ_2). Once again, matching circuits were employed to achieve a larger bandwidth, as the plain structure on its own gave a relatively small bandwidth. From Table 6-2, it can be observed that a larger gap provided a 6 MHz increase in bandwidth.

Table 6-2. Bandwidth comparison for different capacitance cut

Design Case	Start Frequency [MHz]	End Frequency [MHz]	Bandwidth [MHz]
No cut (3.5mm air gap)	824.4	860.4	36
0.5mm cut (4mm air gap)	826.0	863.6	37.6
1mm cut (4.5mm air gap)	821.6	854.4	32.8
1.5mm cut (5mm air gap)	835.6	867.6	32
2mm cut (5.5mm air gap)	823.6	860.8	37.2
2.5mm cut (6mm air gap)	832.4	874.4	42

The S parameters for the different strip widths are shown in Figure 6-4. The 1.5 mm cut (5 mm air gap) and the 2.5 mm cut (6 mm air gap) in the strip width were selected primarily because the former was used in the TCM analysis in Chapter 5, whereas the latter gave the highest bandwidth after matching (7.068 pF and 5.69 nH for the components in Figure 6-2) and also came very close to the capacitance cut used in [7]. Both unmatched cases show resonance at around 810 MHz and 860MHz, similar to the modal resonances in Figure 5-1.

Of the parameters that gave the largest bandwidths in Table 6-1 and Table 6-2, the ones in Table 6-2 (feed position at 22 mm and 2.5 mm capacitance cut) were more suitable, as the feed position corresponds to the shorting pin position used in the TCM analysis in Chapter 5. Moreover, it was observed that in this shorting pin position, almost all characteristic modes had an ECC value of 0.9 or higher. This also reveals that the initial feed position employed in [7] is also valid and applicable to this work.

From the unmatched case in both Figure 6-3 and Figure 6-4, we can conclude that the resonant frequencies for the CST simulations were very close to those of the TCM analysis. This suggests that if the T-strip structure with all components can be further improved to provide better bandwidth performance in λ_1 and λ_2, then it would be possible for antenna feeds to be designed to provide a larger bandwidth, approaching that achieved without components in [7].

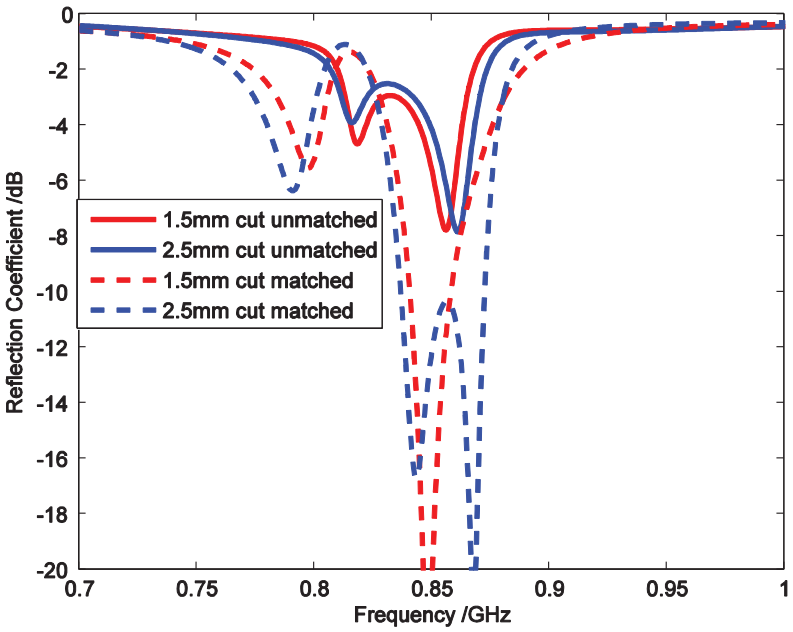

Figure 6-4. S-parameters for the low frequency for both matched and unmatched case at 1.5 mm and 2.5 mm.

6.2 Simulations at High Frequency

The high frequency analysis was done based on the low frequency simulation results, i.e., only the low frequency cases that gave more than 40 MHz bandwidth were considered. The cases of 16 mm and 22 mm feed points were simulated. In each case, a different matching circuit to the one used in the low frequency case was required to obtain enough bandwidth for high frequency operation.

Table 6-3. Bandwidth (BW) for both the feeding point of 16 mm and 22 mm for both the reduced and unreduced capacitance

Design	Start Frequency [MHz]	End Frequency [MHz]	Bandwidth [MHz]
16 mm Feed point	1745.9	1864.2	118.3
22 mm Feed point (no cut)	1727.0	1874.0	147.0
22 mm Feed point (2.5 mm cut)	1731.9	1880.3	148.4

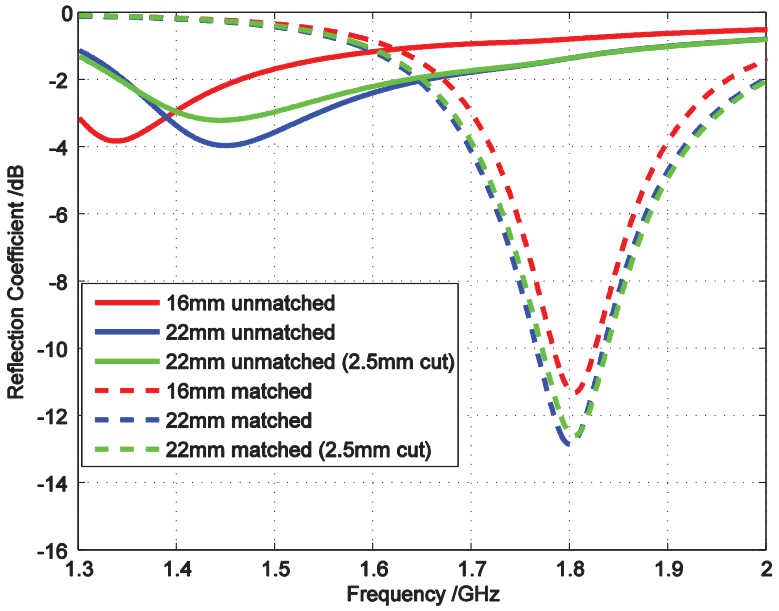

Figure 6-5. S parameters of the unmatched and matched cases for the high frequency.

Two important observations from Figure 6-5 are:

1. Altering the position of the feed point causes a shift in the resonant frequency of the T-strip antenna as shown by the two unmatched plots. In the TCM analysis in Chapters 3 and 4, it was observed that the shorter arm of the T-strip is responsible for the high frequency behavior whereas the longer arm is responsible for the low frequency

behavior. Thus, altering the position of the feed point affects the physical and subsequently the electrical length of the antenna formed. The 16 mm feed point gives an increase in the overall length of the shorter strip (44 mm) compared to the 22 mm feed point (38 mm in length). Thus, the 16 mm feed point is likely to resonate at a much lower frequency (i.e., 1.34 GHz) than the 22 mm offset (i.e., 1.45 GHz) for the unmatched case.

2. Given the same feed position (22 mm), there is no significant difference in the resonant frequency of the high frequency for both matched and unmatched cases (when comparing with vs without 2.5 mm cut) despite the fact that two different tuning circuits were employed. This further supports the argument made in [7] and also in Chapter 5, that altering the longer arm of the T-strip influences the low frequency and has no effect on the high frequency. Both matching cases for the 22 mm feed position (with vs without 2.5 mm cut) have approximately the same starting and ending frequency and for that matter the same bandwidth.

6.3 Summary

In both the low and high frequency cases, it has been shown that there is a high correlation between the characteristic mode behavior of a structure and the behavior of an antenna that can be created from the structure. That is, when cleverly exploited, TCM analysis correctly gives the potential resonant frequency of a structure for antenna design and applications.

However, since the maximum bandwidth obtained in the low frequency case is less than 60 MHz, (the minimum required for LTE applications), further efforts to improve the bandwidth as well as experimental verification are left for future work.

CHAPTER 7

7 Conclusions and Future Work

In this thesis, the characteristic modes of a mobile phone chassis structure were analyzed when it was fitted with different internal components (camera, microphone, battery and screen). It was found that the mode of the structure with the individual components were highly correlated (ECC > 0.9) with their equivalent modes for a plain chassis structure. However, the analysis of the structure with all four components revealed that the two modes obtained by the addition of the T-strips (λ_1 and λ_2) at the low frequency had experienced more significant shifts in their resonant frequencies, despite still having ECC values greater than 0.9. Variation of the capacitance gap was employed to restore the modes to their original resonant frequencies as well as to obtain a 6 MHz increase in the bandwidth of the T-strip antenna when a tuning circuit was applied. Moreover, it was observed that the introduction of the internal components did not affect the fundamental mode (λ_3) obtained as a result of the shape and size of the chassis.

Furthermore, it has also been shown that when properly excited, the resonant frequencies of the characteristic modes in TCM analysis for a particular structure is the same as the resonant frequencies obtained when an appropriate feed is applied to the same structure using CST simulation. For the feed design, one of the shorting pins placed with a 50-ohm feed and the T-strip antenna was optimized for bandwidth by varying the feed positions. Placing the feed at 16 mm from the center of the chassis' longer edge gave the largest bandwidth of 42 MHz. Similarly, keeping the feed point at 22 mm and increasing the capacitance gap between the strip and the chassis also gave more than 40 MHz in bandwidth for the low frequency case. In both cases, the resonant frequencies of the matched circuits for two narrow-band resonances were found to be 810 MHz and 860 MHz. These were the same as the resonant frequencies obtained for λ_1 and λ_2 in the final structure used in the TCM analysis.

By obtaining same resonant frequencies as in the TCM analysis as in the CST simulation, it is shown that characteristic mode analysis can be employed in

antenna design in future mobile handset even with its internal components in place. By proper excitation of the modes with-designed antenna feeds, it is possible to obtain an additional antenna that excites the chassis without being coupled to the traditional antenna that also excites the chassis, enabling efficient MIMO antenna implementation in mobile handsets. Thus, TCM provides a powerful analysis tool for determining the best place of exciting the inherent modes in a structure for antenna synthesis.

Since the minimum bandwidth of 60 MHz required for LTE applications was not obtained with the simulated T-strip antenna, no attempt was made to fabricate a prototype of the entire design. Thus, one important future work is to attempt different structural modifications than the T-strip antenna employed in the thesis, in order to achieve better bandwidth performance. Another important aspect that is left for future work is that different matching circuits were required in this thesis for the low and high frequency cases, even though the same feed was used for both cases. Thus, aside from designing new structural modifications, the matching circuit should be designed to work for both the low and high frequencies.

References

[1] B. K. Lau, "Multiple antenna terminals," in *MIMO: From Theory to Implementation*, C. Oestges, A. Sibille, and A. Zanella, Eds. San Diego, CA, USA: Academic, 2011, pp. 267–298.

[2] E. Dahlman, S. Parkvall, and J. Sköld. *3G Evolution: HSPA and LTE for Mobile Broadband*. Academic Press, London, 2008.

[3] M. Cabedo, E. Antonino, A. Valero and M. F. Battaller, "The theory of characteristic modes revisited: A contribution to the design of antennas for modern applications," *IEEE Antennas Propag. Mag.*, vol. 49, no. 5, pp. 52-68, Oct. 2007.

[4] R. J. Garbacz and R. H. Turpin, "A generalized expansion for radiated and scattered fields," *IEEE Trans. Antennas Propag*., vol. AP-19, pp. 348-358, May 1971.

[5] S. K. Chaudhury, W. L. Schroeder, and H. J. Chaloupka, "Multiple antenna concept based on characteristic modes of mobile phone chassis," in *Proc. 2nd Europ. Conf. Antennas Propag. (EuCAP'2007)*, Edinburgh, UK, Nov. 11-16, 2007.

[6] H. Li, Z. Miers, and B. K. Lau, "Design of orthogonal MIMO handset antennas based on characteristic mode manipulation at frequency bands below 1 GHz," *IEEE Trans. Antennas Propag*., vol. 62 no. 5, pp. 2756-2766, May 2014.

[7] Z. Miers, H. Li, and B. K. Lau, "Design of bandwidth enhanced and multiband MIMO antennas using characteristic modes," *IEEE Antennas Wireless Propag. Lett*., vol. 10, pp. 290-293, 2011.

[8] Q. Guo, R. Mittra, F. Lei, J. Ju and J. Byun, "Interaction between internal antenna and external antenna of mobile phone and hand effect," *IEEE Trans. Antennas Propag*., vol. 61, no. 2, pp. 862-870, Feb. 2013.

[9] R. F. Harrington and J. R. Mautz, "Theory of characteristic modes for conducting bodies," *IEEE Trans. Antennas Propag*., AP-19, pp. 622-628, Sep. 1971.

[10] R. Martens, E. Safin and D. Manteuffel, "Inductive and capacitive excitation of the characteristic modes of small terminals," in *Proc. Loughborough Antennas Propag. Conf. (LAPC'2011)*, Loughborough, UK, Nov. 14-15, 2011.

[11] H. Li, Z. Miers, and B. K. Lau, "Generating multiple characteristic modes below 1 GHz in small terminals for MIMO antenna design," in *Proc. IEEE APS-URSI*, Orlando, FL, USA, Jul. 7–13, 2013, pp.180-181.

[12] Z. Miers, H. Li, and B. K. Lau, "Design of multi-antenna feeding for MIMO terminals based on characteristic modes," in *Proc. IEEE APS-URSI*, Orlando, FL, USA, Jul. 7–13, 2013, pp. 182–183.

[13] K. L. Wong and T. W. Kang, "Internal mobile phone antenna array for LTE/WWAN and LTE MIMO operations," *Microw. Opt. Technol. Lett.*, vol. 53, pp. 1569-1573, Jul. 2011.

[14] S. N. Makarov, *Antenna and EM Modeling with Matlab*. John Wiley and Sons Inc., 2002.

[15] K. J. Kim, S. Lee, H. J. Jung and Y. J. Yong, "Small antenna with a coupling feed and parasitic elements for multiband mobile applications," *IEEE Antennas Wireless Prog. Lett.*, vol. 10, pp. 290-293, 2011.

[16] MNW Scan Pte Ltd, Singapore, "BetaMatch," [Online]. Available: http://www.mnw-scan.com

[17] R. G. Vaughan and J. B. Andersen, "Antenna Diversity in Mobile Communications," *IEEE Trans. Veh. Technol.*, vol. 35, pp. 135 – 145, May 1986.

List of Figures

List of Tables

List of Acronyms

BW	Bandwidth
CC	Correlation Coefficient
CDMA	Code Division Multiple Access
CMOS	Complementary Metal Oxide Semiconductor
CST	Computer Simulation Technology
ECC	Envelope Correlation Coefficient
ESA	Electrically Small Antennas
LTE	Long Term Evolution
MIMO	Multiple Input Multiple Output
MS	Modal Significance
PEC	Perfect Electric Conductor
SNR	Signal to Noise Ratio
TCM	Theory of Characteristic Modes
UWB	Ultra-wide Band

LUND
UNIVERSITY

Series of Master's theses
Department of Electrical and Information Technology
LU/LTH-EIT 2015-465

http://www.eit.lth.se